ΠΟΛΥΤΕΧΝΕΙΟ ΚΡΗΤΗΣ
ΣΧΟΛΗ ΜΗΧΑΝΙΚΩΝ ΠΑΡΑΓΩΓΗΣ & ΔΙΟΙΚΗΣΗΣ
ΕΡΓΑΣΤΗΡΙΟ ΜΙΚΡΟΚΟΠΗΣ & ΚΑΤΑΣΚΕΥΑΣΤΙΚΗΣ ΠΡΟΣΟΜΟΙΩΣΗΣ

Design of a Regenerative Shock Absorber for electric mountain bikes

Δημήτριος Μουμουγιάννης

ΕΠΙΒΛΕΠΩΝ: Παναγιώτης Αλευράς

Εξεταστική επιτροπή:

Καζασίδης Εμανουήλ

Σταυρουλάκης Γεώργιος

ΑΡ. ΔΙΠΛ.: 140

ΧΑΝΙΑ 2025

Contents

1. Introduction

1.1 Background and Motivation

The dawn of the 21st century has witnessed sustainable means of transportation. Within this evolving landscape, electric bicycles have emerged as an alternative solution, bridging the gap between traditional cycling and motorized transport. E-bikes are equipped with an integrated electric motor, which provides pedal assistance, offering a wide range of benefits that appeal to a diverse user base [1]. They extend the range and accessibility of cycling by reducing the physical effort required, thereby making commutes less strenuous, enabling longer recreational rides, and providing access to cycling for individuals who might otherwise be limited by age, fitness level, or challenging terrain.

Beyond urban commuting, e-bikes have also permeated the realm of recreational and competitive sports, most notably in disciplines like enduro mountain biking. Enduro riding, characterized by challenging descents, technical trails, and demanding climbs, places significant stress on both the rider and the equipment. For these applications, robust and efficient suspension systems are not merely a luxury but an indispensable need. A well-designed suspension system in an enduro e-bike plays a critical role in ensuring rider's comfort and safety by absorbing shocks and vibrations from uneven terrain. More importantly, it provides enhanced control and stability, allowing the rider to maintain traction, navigate obstacles effectively, and push the limits of performance on aggressive trails. Without adequate suspension, the riding experience would be jarring, unsafe, and ultimately, limited in its potential.

The development of regenerative shock absorbers for e-bikes, addresses a multifaceted need [2]. This challenge combines mechanical engineering, dynamics, electrical engineering, to create a more intelligent and sustainable mobility solution. The aim of this research is to transform the traditional passive role of a shock absorber into an active component that contributes to the overall energy management of the e-bike, leading to a more efficient, autonomous, and capable riding experience.

1.2 Problem Statement

While it is common for other electric vehicles to recharge via regenerative breaking, bicycles lack any mechanism for energy recovery [3]. For an electric bicycle, which relies on an onboard battery to provide propulsion assistance, this inefficiency influences the e-bike's functionality in multiple aspects:

- **Reduced Battery Range**: Every watt-hour dissipated as heat could have contributed to the e-bike's autonomy. This directly results in a reduced effective riding range, limiting the feasibility of longer commutes or recreational rides, particularly on mountain trails.
- **Inefficient Energy Management**: The e-bike's battery system is designed to provide power, yet a significant source of mechanical energy from suspension movement is entirely disregarded. This represents an inefficiency in the overall energy management strategy of the vehicle.

The field of regenerative solutions for bicycle suspension remains largely nascent. While the concept of regenerative suspension has been explored and implemented to varying degrees in larger vehicles, its application to bicycles is far less developed. The primary limitations preventing widespread adoption of such systems in bicycles include:

- **Severe Space and Weight Constraints:** Bicycles are inherently lightweight and compact. Integrating the necessary mechanical and electrical components for energy

harvesting without significantly increasing the bike's overall weight or altering its geometry poses a major engineering challenge.

- **Low Power Density and Efficiency:** The typical range of motion and forces experienced by bicycle suspension systems are considerably smaller than those in larger vehicles. This makes it challenging to design a regenerative system that can efficiently harvest a meaningful amount of power, with many existing concepts struggling with low conversion efficiency at these scales.
- **Cost and Manufacturability**: Any feasible solution must be produced at a reasonable cost, especially for consumer-grade e-bikes.

Therefore, the problem this thesis addresses is the energy inefficiency within conventional e-bike shock absorbers. The objective of this research is to develop an active energy recovery, compact, manufacturable, prototype absorber which can achieve the goal of extending battery autonomy and improving overall energy efficiency for enduro E-bikes

1.3 Research Objectives

The specific objectives of this research are outlined as follows:

1. To conduct theoretical analysis of energy recovery systems in suspension applications. This involves understanding the principles behind converting mechanical vibrations into usable electrical energy, with a focus on systems applicable to bicycle kinematics.
2. To develop and refine simulation model for the e-bike's suspension system in a multi-body dynamics environment (ANSYS) . This objective includes accurately modeling the bicycle frame kinematics, mass distribution, and conventional damping characteristics (derived from experimental telemetry) to predict the theoretical energy harvesting potential under various road conditions.
3. To design a compact and manufacturable prototype of the regenerative shock absorber using Computer-Aided Design. This design phase will prioritize fitting the absorber within existing bicycle frame constraints, selecting appropriate components, and ensuring the feasibility of fabrication using standard workshop techniques.
4. To construct an experimental prototype of the designed regenerative shock absorber. This objective involves the physical fabrication and assembly of the mechanical and electrical components.
5. To experimentally evaluate the performance. This involves installing the prototype on a standard bicycle chassis, performing controlled tests (e.g., "drop off a step"), collecting empirical data on generated voltage, power output, and overall damping characteristics, and comparing these results against the theoretical predictions from the simulation.

2. Theoretical Background

2.1 Bicycle Suspension Systems

Bicycle suspension systems are engineered to absorb impacts from terrain irregularities, maintaining tire contact with the ground, and enhancing comfort, control, and performance of the rider. In the demanding field of enduro mountain biking, where high speeds meet technical obstacles, a sophisticated suspension setup is required. Nowadays, e-bikes in this category incorporate these systems to manage additional weight and forces associated with their integrated motor and battery systems.

2.1.1 Types of shock absorbers and suspension systems

Bicycle shock absorbers can be broadly categorized by their spring type, each offering distinct advantages and characteristics. The two main types of modern bicycle suspension are coil springs and air springs.

- **Coil Spring** [4]**:** These systems utilize a metal coil that compresses to absorb energy. The primary advantage is a highly linear and consistent spring rate throughout the travel, leading to a predictable and supple feeling. This linearity often provides excellent compliance through small bumps and a 'planted' feeling, which can be beneficial in aggressive enduro riding where consistent traction is crucial. The force exerted by the spring is directly proportional to its displacement, a relationship described by **Hooke's Law** [6]:

$$F = kx \quad (1)$$

  Where:
  - F represents the force exerted by the spring.
  - k stands for spring rate (or stiffness), a constant unique to each spring.
  - x stands for displacement of the spring from its equilibrium position.

  Coil shocks are also generally simpler mechanically, more durable, and less prone to performance changes due to temperature fluctuations. However, they are typically heavier than air shocks, offer limited adjustability (requiring spring swaps to change spring rate), and lack the progressive ramp-up, often desired, at the end of the stroke for harsh impacts, unless combined with hydraulic bottom-out control.

- **Air Spring** [5] **:** Air springs use compressed air within a sealed chamber to act as the spring. Their main benefits lie in their light weight and high degree of adjustability. Air pressure can be easily adjusted with a pump to fine-tune the spring rate for different rider weights and preferences, making them versatile. The principle of operation is based on Boyle's Law [7], which states that for a fixed amount of gas at a constant temperature, pressure and volume are inversely proportional.

$$P_{initial}V_{initial} = P_{final}V_{final} \quad (2)$$

  Where:
  - P refers to pressure
  - V stands for volume

  As the suspension compresses, the air volume inside the chamber decreases, causing the pressure to increase exponentially, which creates a progressively stiffer spring curve, helping to resist bottom-out on large impacts, a desirable characteristic for enduro riding. However, air shocks can sometimes feel less sensitive to small bumps, and their performance can be influenced by temperature changes, as the air density changes. Their sealing systems are also more complex, requiring more maintenance.

Linkage Designs

Beyond the spring type, the way that rear wheel moves and the suspension system reacts to pedaling, braking and vibration forces, depends on the kinematic design of rear suspension.

These linkage designs are complex systems of pivots and links that dictate the rear wheel's axle path. While numerous designs exist (e.g., VPP, DW-Link, FSR, Maestro), they generally fall into subcategories based on their pivot location [8]:

- **Single Pivot:** These are the simplest designs, featuring one main pivot point for the swingarm. While lightweight and easy to maintain, they can exhibit more unwanted interaction with pedaling and braking forces, potentially leading to 'pedal bob' (suspension compression during pedaling) which leads to energy loss or brake squat [9].
- **Multi-Linkage:** These designs use multiple links and pivot points to create a more sophisticated axle path and leverage ratio curve. This allows engineers to finely tune characteristics such as anti-squat (resistance to pedal bob), anti-rise (resistance to brake squat) [32], and progressive or regressive spring curves. The majority of modern enduro bikes, including the Trek Slash Gen 5, consist of complex multi-linkage designs (often variations of a four-bar linkage) to optimize performance across diverse riding conditions, balancing pedaling efficiency with plushness and bottom-out resistance. The precise placement of pivot points and the design of the linkage affect the behavior of the shock absorber, directly influencing the forces and displacements available for energy harvesting [10].

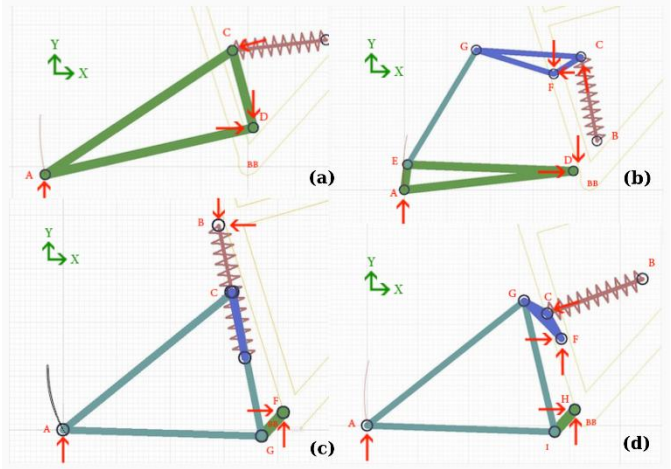

Figure 1: (a)Single Pivot, (b)Four-Bar, (c)Monolink, (d)Virtual Pivot Point (VPP)

Suspension type and linkage design impacts a bicycle's performance, influencing everything, from climbing efficiency to descending capability and overall rider experience. The regenerative shock absorber must fit perfectly with the existing kinematics and react effectively to the specific forces and motions generated by the chosen frame.

2.1.2 Suspension Parameters

A set of major parameters, such as rider's weight, riding style, and specific terrain, are used to fine-tune and evaluate suspension's performance.

Travel and stroke

Travel refers to the total available vertical distance the rear wheel can move, which is a key characteristic, as it changes depending on the bike's category. Stroke on the other hand refers to the maximum linear distance the shock absorber can compress. Enduro bicycles are designed with significant travel (often 150-180mm at the rear wheel) and use shocks with

stroke from 58-65mm, to manage large jumps, drops, and high-speed impacts. Greater travel gives the ability to tune the suspension to be more sensitive at the beginning of its travel and firmer at the end. For a regenerative shock absorber, a longer stroke is beneficial as it provides a greater displacement, facilitating the extraction of more kinetic energy.

Sag

The amount of shock stroke used by the rider's weight when they are in a stationary, riding position. Expressed as a percentage of the total travel, it is the first and most critical adjustment for any suspension system. Sag adjustment depends on rider's weight and riding style. A correctly set sag ensures the suspension has enough travel to extend into dips and maintain tire contact with the ground, while also allowing for full compression on great impacts. In enduro riding, a value between 25% and 30% of the total rear suspension travel is typically considered ideal, balancing climbing efficiency with descending performance.

Spring Rate

Spring rate [11], or spring stiffness, is the force required to compress the spring a given distance. There are three types of spring rate ,Linear, Progressive and Degressive. This parameter directly supports the rider's weight and resists impacts. While a progressive spring rate feels like it provides better support on large impacts, it can sometimes cause a loss of traction due to the increased stiffness. The spring rate must be selected to properly support the rider and absorb energy without feeling too stiff or too soft.

Damping

Damping [12]-[13] is the mechanism that controls the speed at which the suspension compresses and rebounds. It dissipates the kinetic energy of the spring's movement, preventing uncontrolled oscillations (bouncing) after an impact. The two primary types of damping are:

- **Compression Damping**: Controls the rate at which the suspension compresses when a force is applied. It is designed to be progressive, with separate low-speed and high-speed circuits to handle both small bumps and large, sharp impacts effectively.
- **Rebound Damping**: Controls the speed that the suspension returns to full-extended position after a compression. This is critical for preventing the shock from uncontrolled oscillations and launching the rider off the saddle after hitting an obstacle. Rebound must be fast enough to be ready for the next bump but slow enough to maintain control. The physical principle permeates both and describes the hydraulic resistance of fluid passing through a constrained orifice is:

$$F = u \tag{3}$$

F: The compression or rebound damping force exerted by the shock absorber.
c: The damping coefficient
u: The velocity of the piston moves through the fluid.

While in a conventional system, damping converts kinetic energy into heat, the proposed regenerative system introduces an additional electrical damping force that converts the same kinetic energy into electricity, contributing to the overall damping characteristics of the suspension while simultaneously recovering energy.

2.2 Energy Harvesting Principles

2.2.1 Introduction to Energy Harvesting

The concept of energy harvesting [15] entails the capture of ambient energy that would otherwise be dissipated and its conversion into a useful form of electrical power. This principle is becoming increasingly significant, especially with the growth of low-power electronics and the demand for autonomous systems.

The main categories of energy that can be harvested are:

- **Mechanical Energy:** Generated from physical motion, such as vibrations from vehicles, machinery, or even human activity.
- **Thermal Energy:** Derived from temperature differences, this form of energy can be converted using devices like thermoelectric generators.
- **Solar Energy:** The most well-known type of energy harvesting, where light from the sun is converted into electricity using photovoltaic cells.

This study represents an example of harnessing mechanical energy from the vertical motion of a bicycle's suspension, transforming energy that would normally be converted into heat into a useful, electrical form.

Every energy harvesting system, regardless of its source, requires two essential components:

1. **Transducer:** This is the core mechanism that converts one form of energy into another. For example, a water turbine transforms the potential and kinetic energy of water into the rotational motion of a generator, which then produces electricity. Similarly, the system presented here transforms the kinetic motion of the shock absorber into rotational energy and then into electrical energy.
2. **Power Management and Storage System:** Once the energy is converted, it must be properly managed, stored (e.g., in a battery or capacitor), and delivered to the load with minimal loss. An efficient storage system is really important to maximize the amount of the harvested energy.

2.2.2 Operating Principles and Existing Technologies of Regenerative Shock Absorbers

Regenerative shock absorbers [14] represent a specific application of energy harvesting. In contrast conventional shock absorbers serve only to dampen oscillations by converting mechanical energy into thermal energy through fluid friction.
The concept relies on either replacing or supplementing the traditional damping mechanism with an energy conversion device. As the suspension undergoes compression and rebound, the relative motion between the vehicle's chassis and the wheel is utilized to drive a generator. This generator then converts the mechanical into electrical energy from the suspension's articulation, which can be stored or used to power onboard electronic subsystems.
Several technological approaches have been explored for regenerative shock absorbers, primarily in the automotive industry, with limited application to bicycles:

- **Hydraulic-Electric Regenerative Dampers** [17]**:** These systems use the hydraulic fluid flow within the shock absorber to drive a small hydraulic motor, which in turn powers an electric generator. While effective, this approach can add significant complexity and mass to the system, making it less suitable for weight-sensitive applications like bicycles.

- **Electromagnetic Regenerative Dampers (Linear or Rotary)**[16]**:** This is one of the most prevalent and relevant approaches. It achieves the direct conversion of linear suspension motion into electrical energy via electromagnetic induction. This can be done with a linear generator (where a coil moves relative to magnets) or, more commonly, by using a mechanical transducer like a rack-and-pinion assembly to convert the linear motion into a rotary motion that drives a conventional electric motor/generator.

- **Piezoelectric Regenerative Dampers** [18]**:** These systems implement piezoelectric materials that generate an electrical charge in response to mechanical stress. While they are compact and lightweight, their power output is generally very low, making them suitable only for low-power applications such as sensors. They cannot be capable to charge an e-bike's main battery.

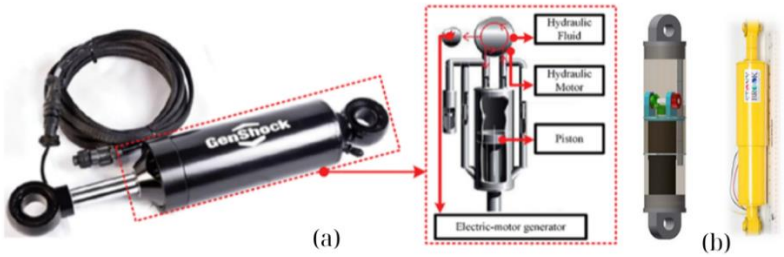

Figure 2:(a) Hydraulic-Electric Regenerative Dampers , (b) Electromagnetic Regenerative Dampers (Linear or Rotary)

For bicycle applications, especially within the demanding enduro category, the chosen design must not only be capable of harvesting energy but also of preserving the desired damping characteristics of the suspension, without compromising riding quality or adding excessive mass. In comparable prototype systems, gear-driven electromagnetic generators are preferred, as they demonstrate higher energy conversion efficiency when contrasted with hydraulic or piezoelectric.

2.2.3 Energy Conversion Mechanisms

In this case a rack-and-pinion system was selected as the conversion mechanism, using a DC motor operating as a generator through electromagnetic induction.
This mechanism functions according to Faraday's Law of Electromagnetic Induction [19], which states that a changing magnetic field induces a voltage in a conductor. Within a DC motor, the rotational movement of its rotor's coils inside, a magnetic field created by the permanent magnets of the stator, generates a voltage. This is the exact inverse of the motor's typical operation, where an applied current causes the rotor to spin. When connected to an electrical load, this induced voltage compels a current to flow, thereby converting mechanical energy into electrical energy.

$$\varepsilon = -N\frac{d\phi_B}{dt} \quad (4)$$

ε: Induced electromotive force (EMF), measured in Volts (V).
N: The number of turns in the coil. If it is a single conductor, then N=1.
ϕ_B: Magnetic flux is a measure of the total number of magnetic field lines passing through a specific surface. (measured in Weber (Wb))
(−): Introduced by Lenz's Law, indicates that the direction of the induced voltage (and current) opposes the change in magnetic flux that generated it.

Referring to this specific regenerative shock absorber, the energy conversion process is achieved through a multi-stage mechanical-to-electrical system:

1. **Rectilinear-to-Rotary Conversion:** The linear displacement of the shock absorber's shaft is converted into rotary motion. This is achieved through a rack-and-pinion assembly, where the linear movement of the rack turns the connected pinion.
2. **Speed Augmentation:** The rotary motion from the pinion is then transferred through a gearbox with 1: 34.8 gear ratio . It increases the angular velocity of the drive shaft, ensuring that the connected DC motor spins at a speed sufficient to generate a useful voltage.
3. **Electromagnetic Generation:** The augmented rotational speed is delivered to the DC motor's shaft, causing its internal rotor to spin within the magnetic field. This action converts the mechanical input into electrical energy, which is collected at the motor's terminals.

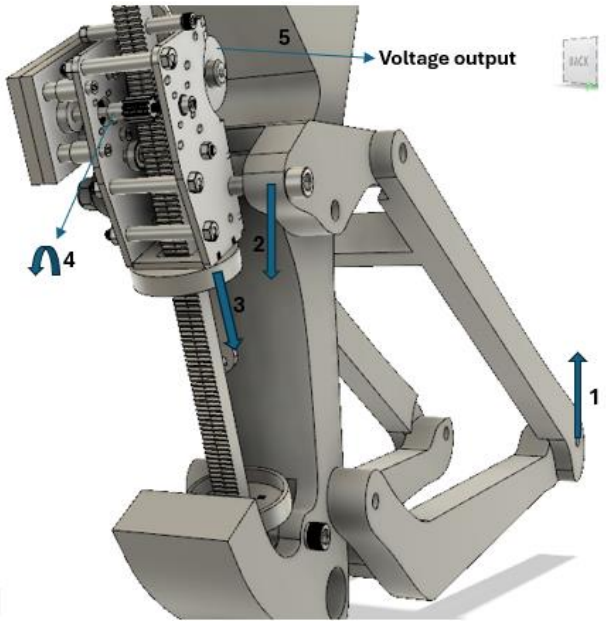

Figure 3:1)Applied Forces, 2,3)Linkage and main-body movement,4)Pinion's rotational movement

2.3 Damping Theory

2.3.1 Viscous Damping

A typical air/oil shock absorber dissipates kinetic energy, converting it into heat. This is achieved via the controlled movement of hydraulic fluid (oil) through a series of internal orifices [20]. The shock absorber is composed of two distinct chambers: an air chamber, which functions as the spring, and a second chamber containing hydraulic fluid. As the suspension is compressed, a piston displaces the oil, forcing it to pass through specifically designed orifices or ports. The resistance to this fluid flow is directly proportional to the piston's velocity, thereby generating a damping force. The hydraulic chamber communicates with an external reservoir, often referred to as "piggy bag", which also contains a piston. This piston separates the oil from a volume of compressed air, preventing cavitation and ensuring consistent damping performance throughout the suspension's full travel. The diameter of the orifices can be adjusted through the rebound and compression settings, allowing the user to customize the damping characteristics to suit their riding style and the terrain.

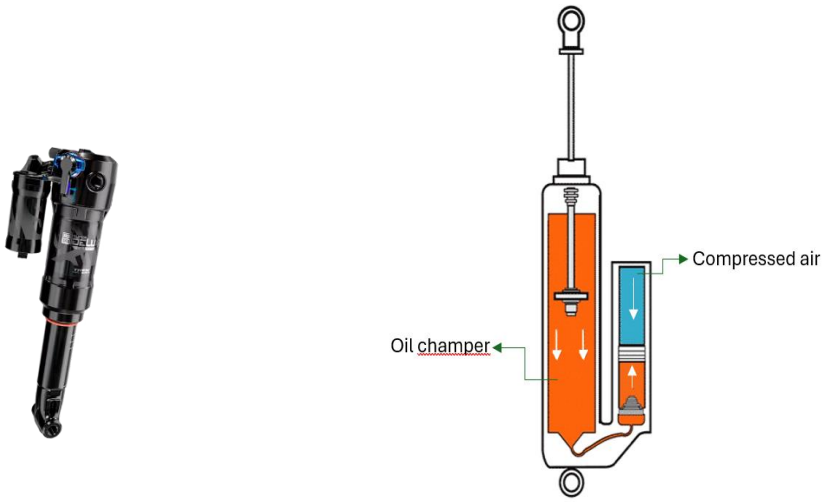

(a) (b)

Figure 4: (a) Air/oil shock ,(b) Function explanation of an air/coil shock

2.3.2 Mechanical Damping

In addition to viscous damping, a suspension system exhibits mechanical damping [21], which arises from friction. This includes sliding friction between the shock absorber's seals, rotational friction within the bearings of the linkage system, and friction from the spring itself. While this form of damping is not as significant as viscous damping, it must be accounted for.

2.3.3 Electrical Damping

In contrast to conventional systems that rely on viscous damping, the proposed regenerative shock absorber introduces an additional, controllable force known as electrical damping [22]-[24]. This force is a direct consequence of the energy conversion process and is linked to the electrical load of the circuit. The generation of electrical energy requires a mechanical power input, which appears as a resistive force opposing the motion of the suspension. This effect is known as back electromotive force (back EMF) [25]-[26].

The total resistance within the electrical circuit has a direct impact on the damping characteristics of the system. It can be adjusted to tune the damping force, allowing for a customized suspension profile.
The advantage of electrical damping over its viscous counterpart lies in its ability to convert kinetic energy into usable electrical power, rather than dissipating it as heat. Furthermore, electrical damping offers the potential for dynamic, real-time control, as the damping force can be adjusted by changing the circuit's electrical load, providing a level of tunability that is not possible with a purely mechanical system.
Regardless of the damping type, the common characteristic among all three is the **damping coefficient** (c) [27], which is calculated according to the corresponding formulation for each case

$$c = 2\zeta\sqrt{K \cdot m} \tag{5}$$

- m stands for mass
- K spring constant (stiffness) in N/m

The damping coefficient is directly related to the **damping ratio** (ζ) [28], which expresses the level of damping relative to the system's critical damping.

$$\zeta = \frac{1}{\sqrt{1 + \left(\frac{2\Pi}{\delta}\right)^2}} \tag{6}$$

ζ < 1: Underdamped - The system oscillates before settling down.
ζ = 1: Critically Damped - The system returns to equilibrium as quickly as possible without oscillating.
ζ > 1: Overdamped - The system returns to equilibrium slowly, without oscillating

The **logarithmic decrement** (δ) [29], is the natural log of the ratio of successive amplitudes in a damped oscillation. It is used to quantify how quickly vibrations decay in underdamped systems. Higher decrement means stronger damping.

$$\delta = ln\left(\frac{A_1}{A_2}\right) \tag{7}$$

2.4 Relevant Electrical Components

2.4.1 DC Motors

The selection of the DC motor [30] for the prototype was based on several key considerations. The motor was already available in the lab, which made it a practical choice for a proof-of-concept prototype. Its size was also a crucial factor, as it needed to fit within the limited space of the bicycle frame. Furthermore, initial bench tests were conducted to evaluate its performance, where a rotational speed was applied to the motor to see its voltage output. The performance in these tests, confirmed its suitability for the project.

A governing principle of this component is the linear relationship between rotational speed and generated voltage -as the angular velocity of the motor's shaft increases, the induced voltage at its terminals increases linearly- a relationship described by Faraday's Law of Electromagnetic Induction.

2.4.2 Rectification and Filtering

The electrical energy produced by a DC motor operating as a generator is not suitable for direct use by an e-bike's battery. Although the motor is designed for direct current, the continuous change in polarity as the rotor spins within the magnetic field results in an alternating voltage signal at the motor's terminals. This AC voltage must first be converted into a stable DC input, to be stored in a battery.
The rectification process is performed by a diode bridge rectifier [31]. This component is a circuit of four diodes that redirects the alternating current so that it flows in only one direction. This action transforms the oscillating AC voltage into a pulsating DC voltage, where all the current is flowing in the same direction, but the voltage level is not constant.
A capacitor is a passive electronic component that stores electrical energy or acts as a filter. In this case it is placed after the rectifier to smooth out the pulsating DC, transforming the signal into a stable, usable DC voltage.

2.4.3 Voltage Dividers

A simple linear circuit that produces an output voltage that is a fraction of its input voltage. It is composed of two series resistors and protects the sensors from high voltage, while scaling it down for accurate measurement. The need for a voltage divider arose because the potential voltage generated by the prototype was significantly higher than the maximum input voltage the INA219 sensor could safely handle. Without this protective circuit, the sensor could be permanently damaged.

2.4.4 Arduino

The Arduino was chosen as the central controller for the prototype's data acquisition system due to its ease of programming, compact size, and compatibility with external modules. Its small dimensions contributed to easy mounting on the bicycle which ensured the necessary autonomy during the experiments.

2.4.5 INA219

The INA219 is voltage and current measurement sensor, making it ideal for energy monitoring applications with microcontrollers as Arduino. The sensor can accurately measure voltages up to 26V on the power bus. Last but not least it communicates via the I2C protocol, simplifying wiring.

3. System Modeling and Simulation

3.1 Bicycle Model Development

3.1.1 CAD Modeling of Bicycle Frame

The first stage of this research was the creation of a realistic and kinematically accurate 3D model of the bicycle frame that would serve as the foundation for all subsequent simulations. This process was executed within Fusion 360 and was initiated by importing a photograph of the subject bicycle in a side-view orientation. To scale the image to its actual dimensions, a calibration procedure was performed by identifying two known points within the photograph and inputting their real distance. This method enabled the creation of an image backdrop with a 1:1 scale, which served as a precise visual guide.

Following calibration, an image tracing technique was applied to meticulously trace the outline of the bicycle's frame and swingarm geometry. The geometric accuracy of the model was further validated and enhanced by incorporating precise specifications obtained from the manufacturer's website, including parameters such as frame reach, head angle, chain stay length, and wheelbase.

Figure 5

A great importance step in this process was the measurement of the exact distances between the center points of the bearings on the suspension linkage. These measurements were taken directly from the physical bicycle to ensure the highest degree of fidelity. This high level of accuracy was essential for two primary reasons: first, to ensure that the kinematic motion of the linkage system would be simulated correctly in ANSYS, and second, to provide a precise framework for the subsequent design of the prototype shock absorber. The produced CAD model is shown in Fig. 6.

Figure 6: Trek Slash gen. 5 2022 Cad Model

3.1.2 Simulation Modeling (ANSYS)

The modeling process began by importing the STEP file of the Cad Model into ANSYS Rigid Dynamics–Mechanical. Once imported, the kinematic structure of the bicycle was defined by establishing joints between moving parts to replicate the mechanical motion of the suspension system.

Rotational joints were created at the following interfaces:

- Between the **chainstay** and the **frame**
- Between the **chainstay** and the **seatstay**
- Between the **seatstay** and the **rocker link**
- Between the rocker link and the frame

Instead of the rear absorber, a spring probe was positioned between the rocker link and the bottom mount of the frame to simulate the rear suspension mechanism. Similarly, a spring probe was applied between the fork stroke and the lower legs to simulate the front suspension absorber These spring probes were defined with stiffness properties from the respective absorbers.

To simulate the interaction of the bicycle with road irregularities, two rigid blocks were inserted under the centers of the front and rear wheel axles. Each block was connected to the corresponding axle via an additional spring probe. Deformation points derived from MATLAB simulations were applied to the blocks with a time delay to account velocity of the bicycle.

The next step in the simulation process following the kinematic modeling of the bicycle frame, was to accurately define the mass and inertia distribution of the system within ANSYS.

The masses of specific components, such as the saddle, seat post, and handlebar (including brake levers, gear shifters, and grips) etc., as well as the fork and the frame itself, were determined using data provided by their respective manufacturers. This approach ensured that the overall mass of the digital model was identical to that of the physical bicycle.

For further refinement, point masses were created and strategically placed at the center of the wheel axles. These point masses represent all the components located nearby, including the

brake rotors, brake calipers, drivetrain, and the complete wheel assembly. The reason to use point masses for these components, rather than modeling them in full detail, was to simplify the computational model without sacrificing accuracy in the dynamic simulation. An additional point mass was also added, as the weight of the crankset, bottom bracket, and pedals, further enhancing the model's precision.
Finally, the rider's weight added as a point mass. The location for this mass was carefully selected to correspond to the point defined by the manufacturer's geometry chart for stand over height. This specific placement ensured that the rider's weight was accurately distributed over the bicycle's frame, a crucial factor for the realistic simulation of suspension behavior and sag

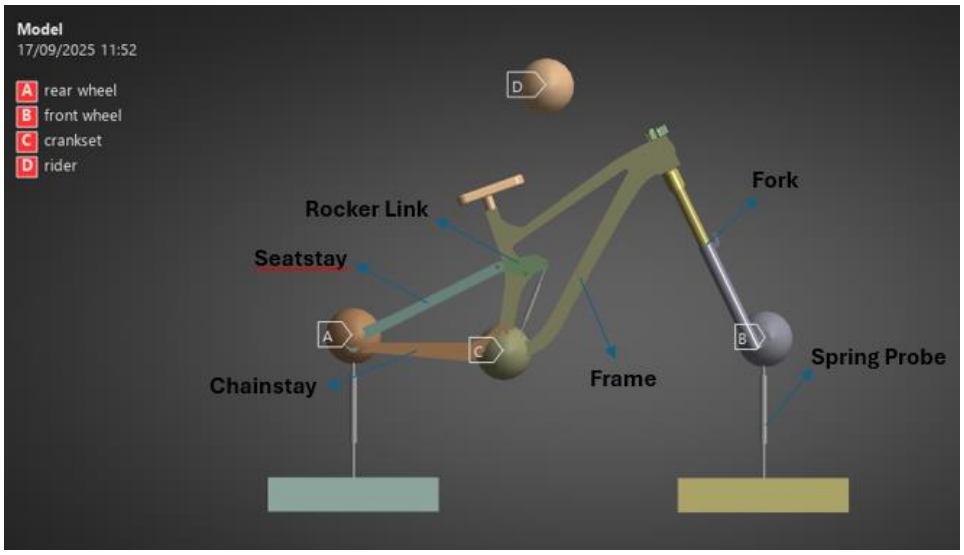

Figure 7: Bicycle model, with point masses added in the ANSYS environment

3.2 Conventional Suspension Characterization

3.2.1 Experimental Setup for video motion analysis

Part of the study was determining the dynamic properties of the suspension experimentally, so an experiment was conducted to determine the damping coefficient of the absorber using motion video analysis. The procedure involved dropping off from a 255mm step with the bicycle while recording the absorber’s response. To eliminate relative motion between the camera and the absorber, the camera was mounted on the same system (bicycle frame) as the suspension. A small red marker was affixed to the absorber, providing a reference point for subsequent tracking within the software. The experiment was repeated three times to enhance reliability and ensure repeatability of the measurements. This approach allowed for the calculation of an average value with improved accuracy by comparing the outcomes of all three trials.
The primary challenge encountered in this phase was ensuring the camera’s view was as parallel as possible to the suspension's line of motion to prevent measurement inaccuracies.
This problem was resolved through a smart design of a custom camera mount. The mount incorporated a three-axis adjustment mechanism, which allowed for precise angular alignment of the camera relative to the suspension linkage.

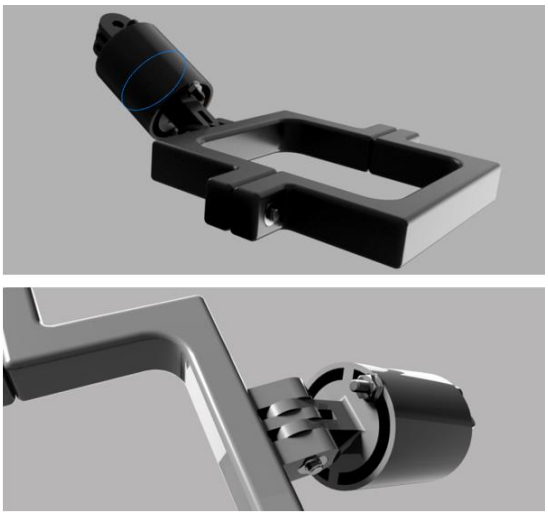

Figure 8: Custom camera mount

Figure 9: Camera mounted on the bicycle frame

This custom mount was 3D printed using PETG filament, a material choice made due to its robustness and ability to withstand the dynamic forces generated by the camera's weight during the test.

3.2.2 Telemetry Data Acquisition and Analysis

Initially, the video was imported into Tracker software for kinematic analysis. Using the calibration stick tool (blue line), the actual distance between two reference points within the video was defined — specifically, the distance between the sag measurement lines along the absorber's stroke. This established a precise 1:1 scale for subsequent measurements. The coordinate system was then configured accordingly (purple cross). A point mass (mass A) was then defined for tracking purposes on the red marker that was affixed to the absorber, providing a high-contrast reference point for the software's pixel-based tracking algorithm. Activating the AutoTrack mode enabled automated frame-by-frame detection of the marker. This process produced the displacement-time graph shown below on the top right side of the Fig. 10.

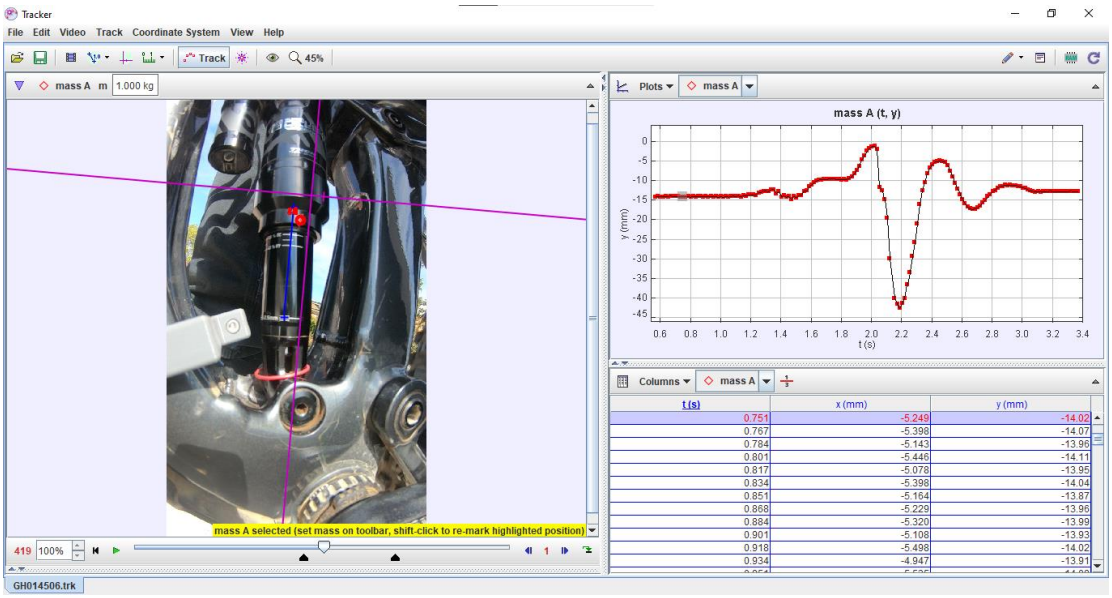

Figure 10:Tracker environment

This process produced the displacement-time graph shown above on the top right side of the Fig. 10.The analysis provided a waveform that captured the suspension's full range of motion, from its initial extended position to its compression and subsequent oscillation.

Theoretical sag value	15.625 mm (25% of stroke)
Stroke	62.5 mm
Step height	255 mm

Figure 11: Set-up process of the axle and calibration stick in Tracker software.

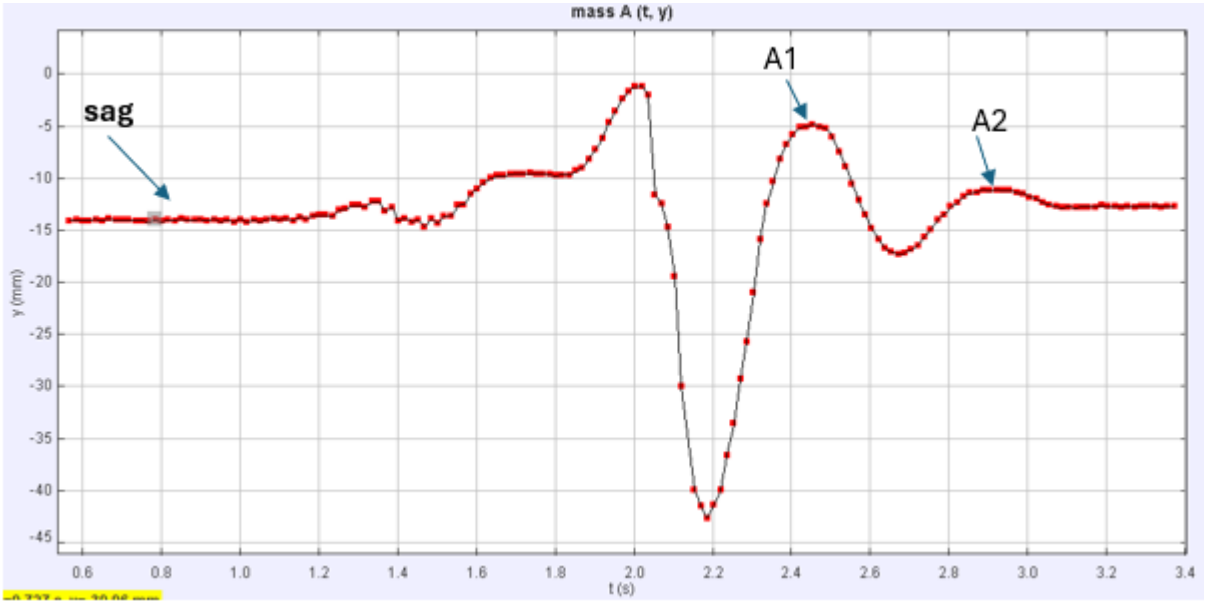

Figure 12: Experiment 1

MAX	MIN	A1	A2
-1.116	-42.6	-4.8	-11.04

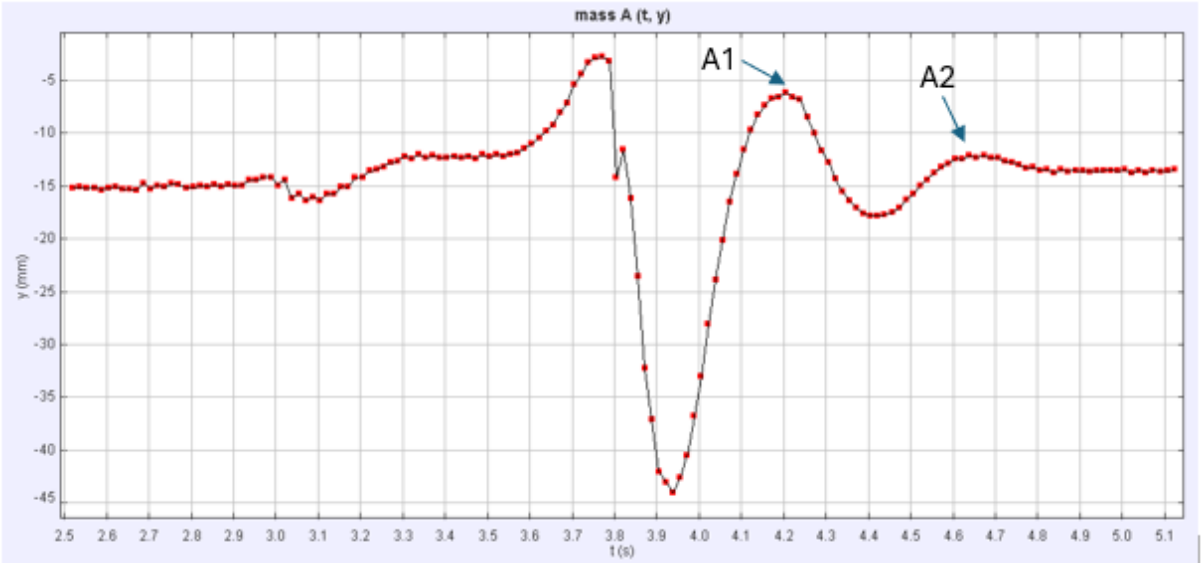

Figure 13:Experiment 2

MAX	MIN	A1	A2
-2.695	-44.01	-6.078	-12.06

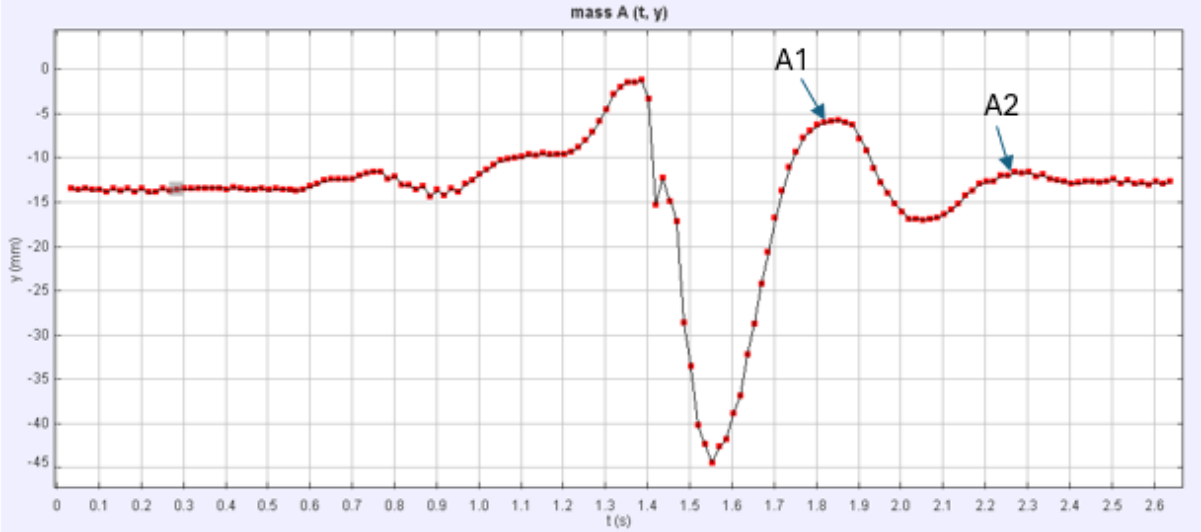

Figure 14:Experiment 3

MAX	MIN	A1	A2
-1.150	-44.43	-5.672	-11.60

Figure 15:Damper fully extended

Figure 16:Damper compressed

3.2.3 Integration of Experimental Data into ANSYS Model

The final step in the modeling phase, was to load the data that extracted into ANSYS simulation in order to tune the suspension parameters. The analysis of this data, included the application of the previously defined logarithmic decrement, provided the necessary values for the damping coefficients, which were then used to refine the ANSYS simulation model.

For K=100N/mm (spring rate)

Compression Damping

Video	Damping ratio (ζ)	Damping Coefficient c(Ns/m)
1	0.131	27.08
2	0.108	22.34
3	0.113	23.31

Rebound Damping

Video	Damping ratio (ζ)	Damping Coefficient c(Ns/m)
1	0.142	50.8
2	0.143	51.11
3	0.151	53.98

This process of experimental validation and subsequent model refinement ensured that the simulation results were not theoretical but were grounded in the observed performance of the conventional suspension system.

3.3 Regenerative System Simulation

3.3.1 Road Profile Generation

A custom script in MATLAB generates road profiles based on the international ISO 8608 standard, which classifies road surfaces into categories ranging from Class A (very smooth, like a new asphalt road) to Class H (extremely rough, like an off-road track). This classification is based on the road's Power Spectral Density (PSD), which measures the way surface irregularities are distributed across different wavelengths. In this study Road Class E is used, representing a highly irregular and unpaved surface, ideal for simulating the demanding conditions of technical enduro trails.

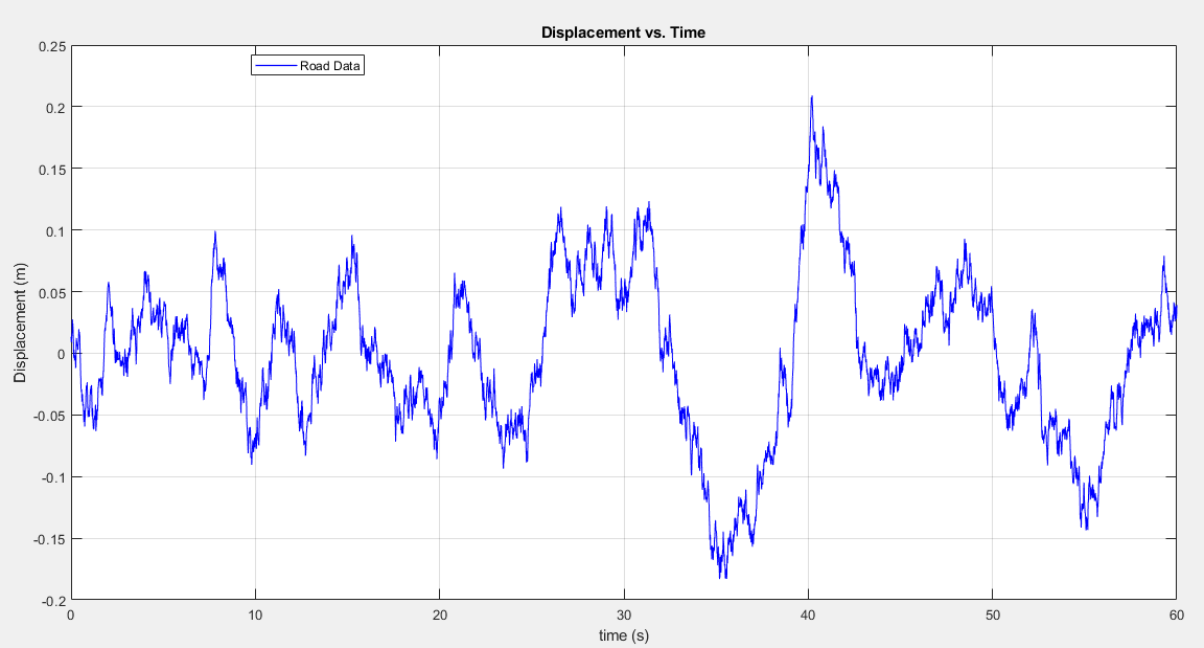

Figure 17:Road elevation time history

The output was a set of elevation points over a specified distance. It was essential to convert data from spatial profile into a time-based profile. This was achieved by defining constant speed for the bicycle (18 km/h or 5 m/s). The script then converted the distance-based elevation into a series of corresponding time-based displacement points.

3.3.2 ANSYS Simulation for Energy Output

From ANSYS, the damping forces were calculated and subsequently multiplied by the suspension compression velocity in order to obtain the damping power. On the right, the corresponding diagram is presented as a function of time. The average value of the results provides the theoretical performance, which was determined to be 75.42 W.

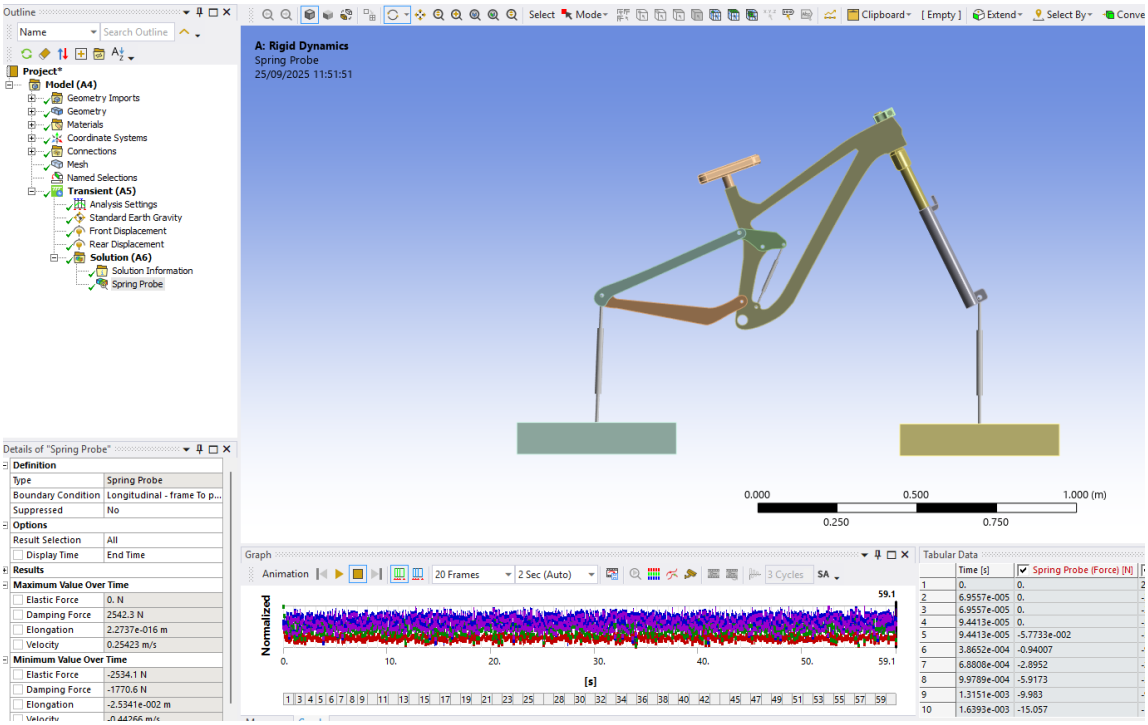

Figure 18:Ansys Simulation

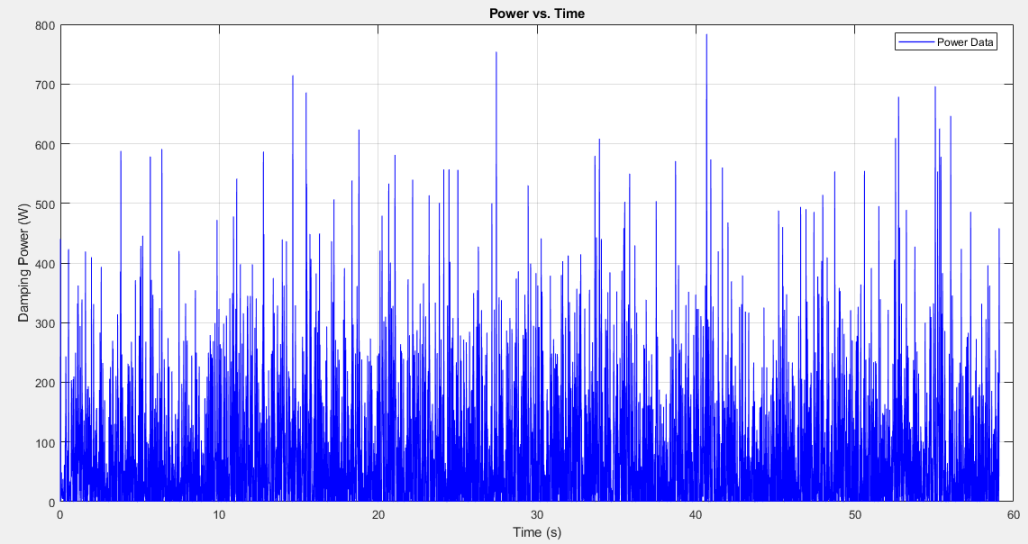

Figure 19:Damping Power vs Time Graph

3.3.3 Electrical Circuit Simulation (Simscape)

Following ANSYS simulations, the final stage of the modeling process was the simulation of the electrical circuit. This was performed using Simscape, a Simulink library. The forces from the rack and the corresponding velocity of the suspension's motion, which were derived from the mechanical simulations, were applied as inputs, to evaluate the voltage output of the regenerative system using a digital probe.

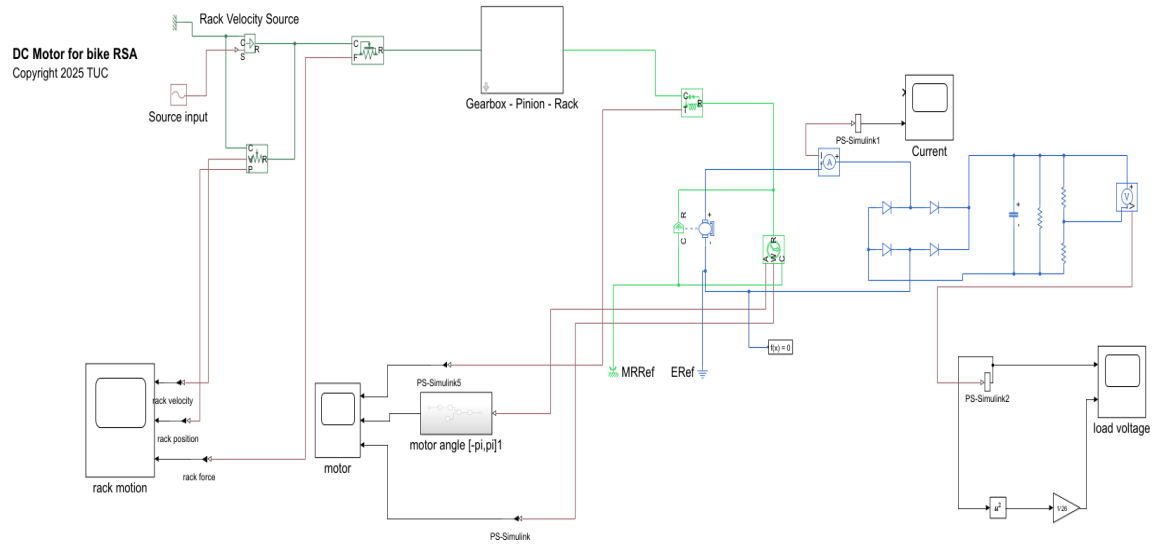

Figure 20: Electrical Circuit

Figure 21: Applied forces

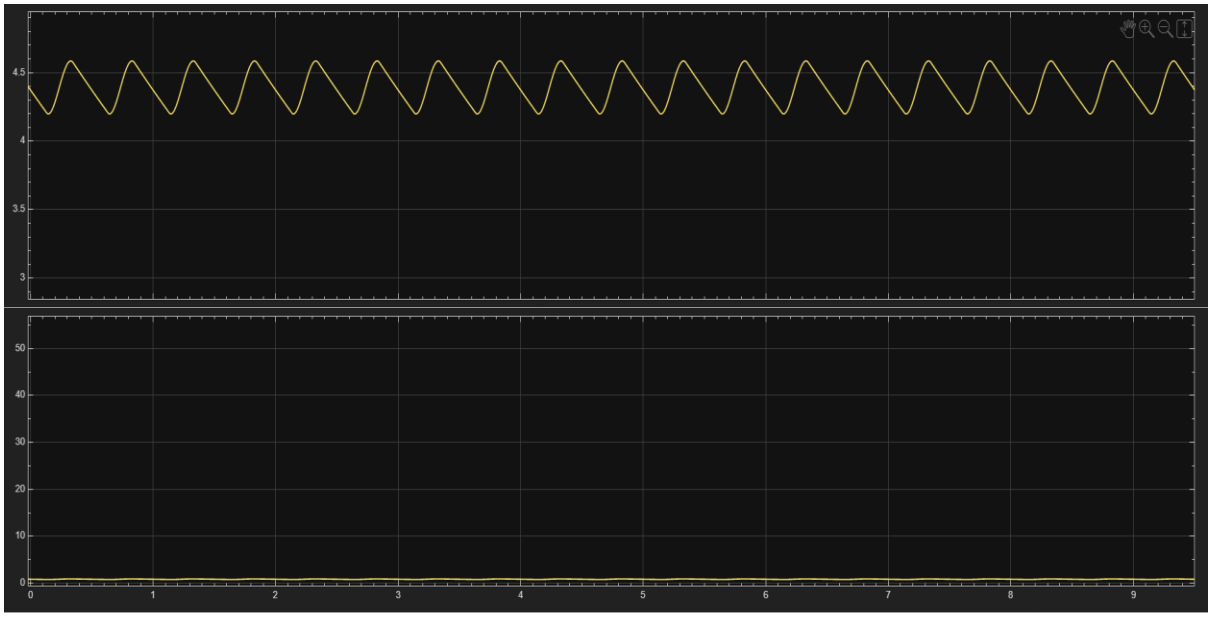

Statistics

PS-Simulink2	Max	Min	Peak to Peak	Mean	Standard Deviation	Median	RMS
Time (s)	7.8310	7.6485					
Value	4.581918402444757 5	4.195741350862089	0.3862	4.3818	0.1262	4.3834	4.3836

Figure 22:Voltage output

4. Design and Construction of the Regenerative Shock Absorber

4.1 Design Constraints and Considerations

4.1.1 Constraints

The prototype had to be designed to fit precisely within the existing frame of the bicycle without protruding beyond its boundaries. The rider's legs should not be obstructed while pedaling. This *spatial limitation* was even more complicated due to the intricate geometry of the rocker link, which is the component that connects the absorber with the bicycle's suspension linkage. Additionally, it should be ensured that the suspension could move freely through its entire travel without contacting any part of the frame at full compression. The design philosophy prioritized *structural integrity* and functionality over weight optimization, given the prototype's purpose as a proof of concept. Thus, the chosen parts were justified by their ability to fulfill the requirements of the regenerative system.

Figure 23

4.1.2 Manufacturability

Engineers should also take into consideration the cost and the manufacturing time of a product. In order to minimize both factors, design's simplicity and the usage of standard workshop techniques (e.g. laser, welding, lathe machining) is preferred. This methodology not only simplified the manufacturing process but also ensured the feasibility of the final prototype. Components were designed to interlock like puzzle pieces, with specific tabs and recesses as shown below in Figure 23, to simplify the welding process due to limited prior experience.

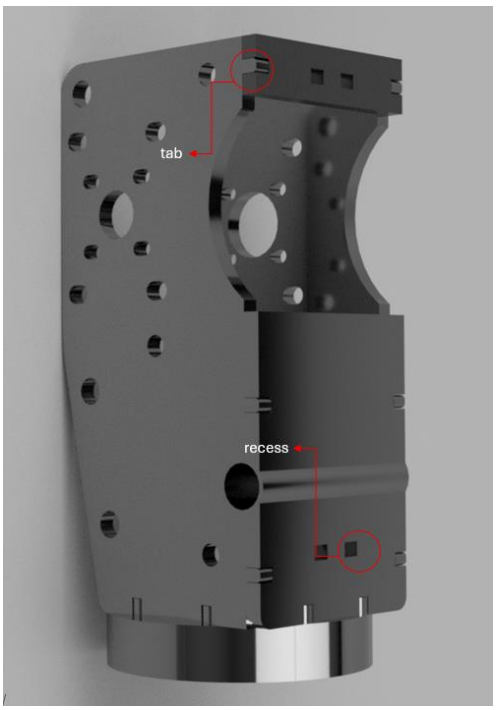

Figure 24

This design choice provided a mechanical guide for alignment, eliminating protentional errors during assembly and welding of the main body. Additionally, custom spacers were fabricated, and bolts were modified on lathing machine to suit the specific needs of the prototype.

4.1.3 Component Selection Justification

Based on the ANSYS output and the forces generated during the simulations, Module 1 was selected for the gear design. This choice was advantageous firstly because Module 1 was the smallest available rack, with 15×15 mm dimensions, satisfying spatial constraints and secondly, it allowed the selection of a small 12-tooth pinion, which, combined with a gearbox ratio of 1:34.8, resulted in a total gear ratio of 34.8 from the rack to the generator, thereby achieving the desired increase in angular velocity necessary for the required damping coefficient.

4.2 Mechanical Design

4.2.1 Detailed Description of the Prototype Design

In Figure 25(a), a bolt with two spacers positioned on either side of the rack functions as the upper stopper of the main body, preventing excessive extension of the absorber. At the rear of the rack, the bearing's guide with a slot which is more visible in Figure 25(c) accommodates the movement of bearings, enabling smooth linear motion of the main body throughout its travel. The slot ensuring precise tangential alignment with the rack. Furthermore, two additional bearings are mounted at the front of the guide, reinforcing positional stability and maintaining the correct orientation of the assembly. Under this arrangement, the pinion achieves smooth and consistent rotation, as all operational loads and reaction forces are efficiently distributed to the bearing system.

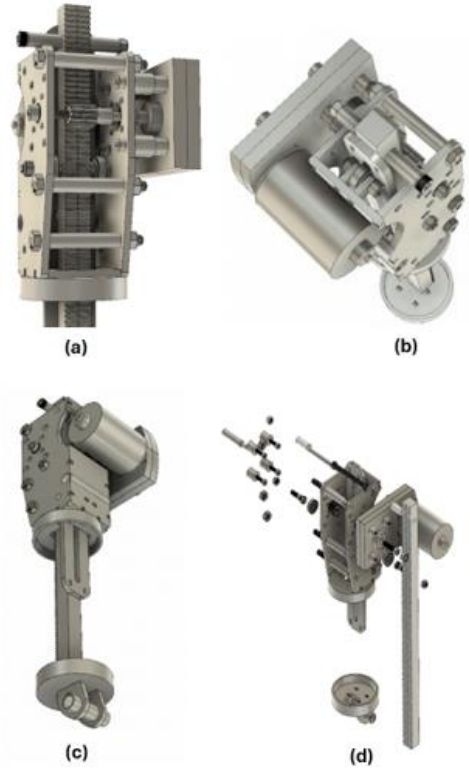

Figure 25: (a)Front view, (b)Top view,(c) Rear view,(d) Exploded View

Figure 26:(a)Bicycle assembly, (b)Absorber compressed

4.3 Electrical System Design and Implementation

4.3.1 Circuit Diagram and Component Selection

The electrical system of the regenerative shock absorber was designed to efficiently convert the energy harvested from the suspension's motion. The core of this system, as depicted in Fig. 27, consists of several interconnected stages to ensure stability and usability of power output.

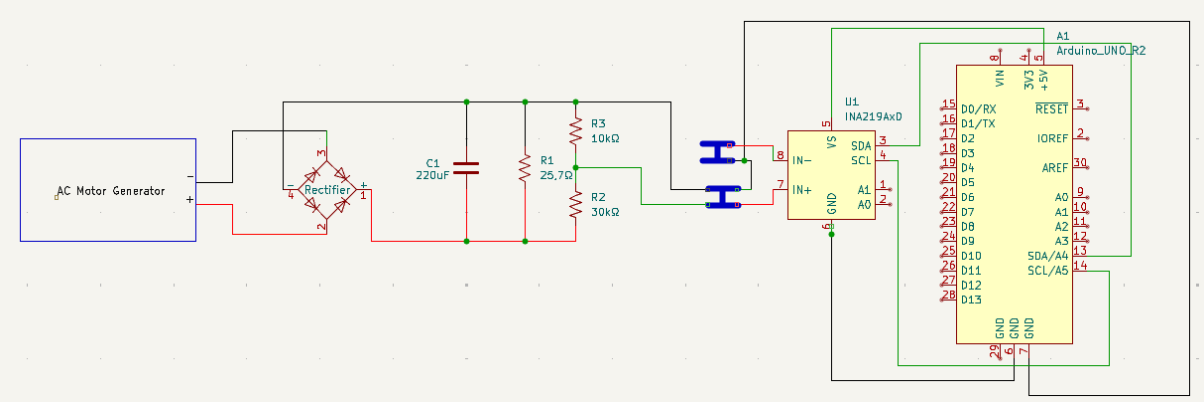

Figure 27:Electrical circuit KiCad design (generator to Arduino)

The process begins with the AC motor generator, which is responsible for converting the mechanical rotational energy from the gearbox into electrical energy. Two wires from the generator are connected to a diode bridge rectifier (rated for 8A, 800V). Rectifier transforms the alternating current (AC) output from the generator into a pulsating direct current (DC). The pulsating DC voltage is routed to a parallel circuit that includes a smoothing capacitor (220μF, 250V) and a resistor, working together to filter, stabilize the voltage signal and provide a more constant and continuous DC output.

Parallel to the capacitor is connected a voltage divider, formed by two resistors (10 kΩ and 30 kΩ). This divider was necessary, firstly to reduce the voltage to a safe level for the connected sensors, thereby preventing damage; and secondly, to provide a precise voltage measurement point. The INA219 connected in series to an Arduino microcontroller. Arduino acts as the brain of the data acquisition system, gathering the data for analysis and validation of the prototype's performance.
To control the damping characteristics of the system, a parallel array of seven 180 Ω resistors (rated at 15W) is used. This configuration created a combined resistance of approximately 25.7 Ω, which, based on the Simscape simulation, provided the desired damping force.
Experimental observations confirmed that a very low circuit resistance created a high back EMF, impeding the suspension's motion. An experimental load of approximately 25.7 Ω, the system's behavior more closely resembled that of the original air suspension.

4.3.2 Microcontroller Arduino

A pivotal element in the system's implementation was the need for autonomous data logging, without a computer connection, as the tests required the bicycle to be in motion. For this purpose, an SD card module was integrated into the circuit. A C++ code was developed specifically to program the microcontroller, setting a very high sampling rate for more accurate results (60 samples per second). The first phase is initialization where the connection and functionality of the sensor and the SD card module are verified. A visual signal, from the built-in LEDs of the Arduino, declares that initialization phase ended and the data logging started, solving the practical challenge of knowing the exact moment of data acquisition. During the logging phase, the LEDs stay on till the end of the predetermined duration. These measurements, along with a timestamp, are directly written onto a CSV file on the SD card. Finally, LEDs turn off stating that the process has ended.

4.4 Prototype Fabrication

At the beginning, the components of the main body were cut using a laser cutter. After removing burrs and cleaning the parts, the main body was assembled, and tack welding was performed on the tabs to ensure the components remained securely in position. Subsequently, TIG welding was applied along all contact points of the main body, and the welds were cleaned using an iron rod, as shown in Figures 28c and 28d.

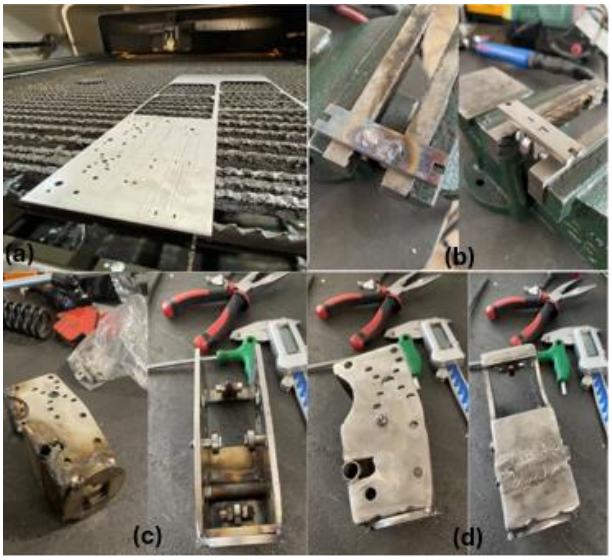

Figure 28

Following this, the rack was welded together with its bottom mount (Fig. 29(a) , Fig. 29(b)) and guide(Fig. 29(d)).

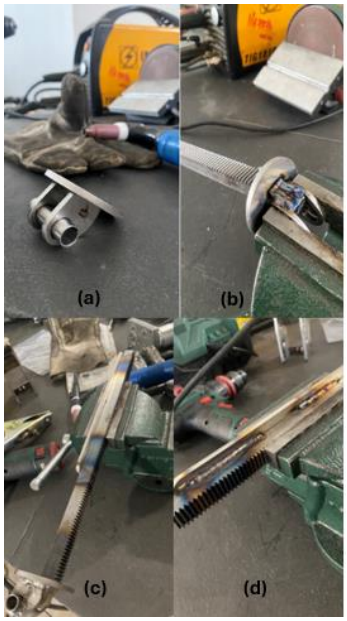

Figure 29

The spacers were then machined on the lathe to their final dimensions. The gearbox axle Fig.30(b) was also machined to achieve an interference fit Fig.30(a) with the pinion. The pinion was machined on one side for interference fitting, while the right side was threaded internally Fig.30(c) to accommodate the right-side axle.

Figure 30

Assembly began with the installation of the bearings into the main body, followed by fastening all bolts. The rack and its guide, already welded together, were first inserted through the coil and positioned beneath the main body, allowing the rack to pass through it. Finally, the gearbox, along with the pinion and axle, was mounted to complete the final assembly as shown in Fig. 31 below.

Figure 31: Final Assembly

5. Experimental Testing and Results

5.1 Experimental Setup

5.1.1 Installation of the Regenerative Shock Absorber on the Bicycle Chassis

After the final assembly, the prototype was installed on the bike. The mounting points aligned precisely with the frame, with no gaps or misfits, and all connections were secure. The system operated smoothly, without any interference between the main body and the frame, or the motor on the rocker link. These results confirmed the accuracy of the CAD design and the effectiveness of the dimensional tolerances applied during the manufacturing process. The circuit was then mounted on the bicycle frame in a way that does not interfere with the rider's movement or the suspension's operation, securing all components and wiring to prevent damage during testing. All connections within the circuit were permanently secured through soldering, ensuring system's reliability.

Figure 32: The bicycle with the absorber installed and the electrical circuit attached on it

5.1.2 Experiment Methodology

As established in 2.3 Damping Theory, there are two different types of damping forces (mechanical and electrical). After the final construction of the design, two experiments were

conducted under the same conditions as in the experiment in 3.2.1 Experimental Setup for video motion analysis. The purpose of these experiments was the determination of mechanical and electrical damping forces.

5.2 Data Analysis

5.2.1 Telemetry Data Acquisition and Analysis

Mechanical

For the first experiment the circuit was not included in the system. In Fig.33, as shown the sag position is 30 mm (48%), which is nearly twice the value compared to the previous experiment. The main result of the experiment is that the oscillations decay rapidly, indicating a high damping coefficient. Furthermore, the absorber never returns to the original sag point, on the contrary it stays compressed a few millimeters under it.

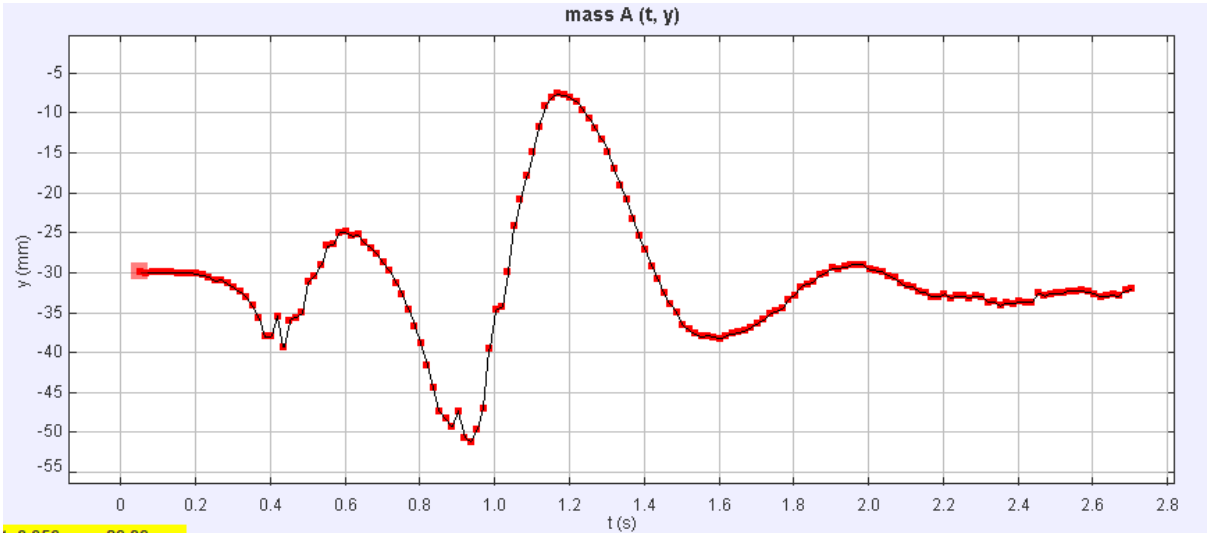

Figure 33: Mechanical Damping Results

The data from this experiment represented by the blue graph in Fig.34 was compared with the results of the ANSYS simulation, shown in the orange graph, and it is evident that the orange graph closely follows the blue one, indicating that the model demonstrates a high degree of accuracy.

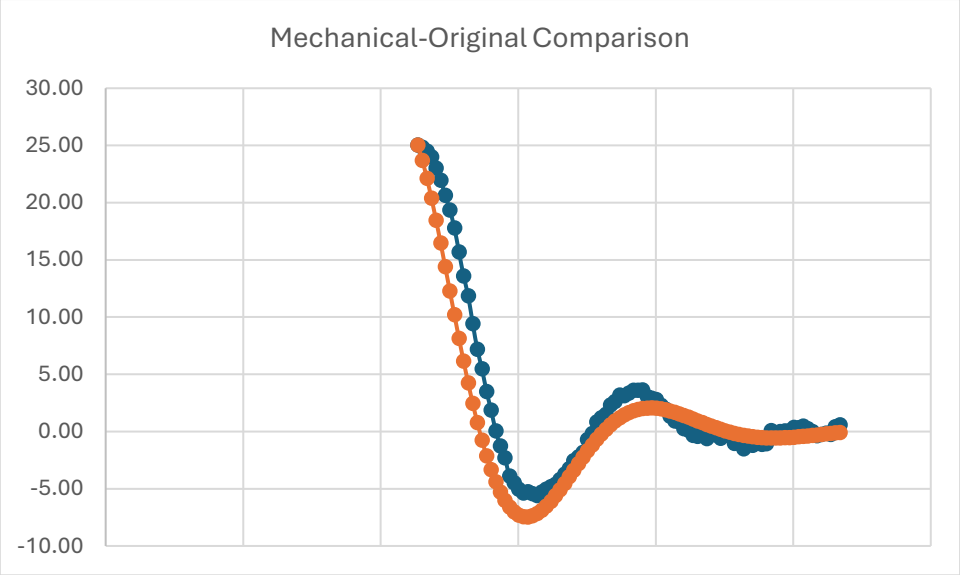

Figure 34

Total Damping (Electrical and mechanical)

In this experiment, the electrical circuit was included in the system. The sag point is higher than the mechanical case (26 mm ~41,6%), as shown in Figure 35: Electrical Damping Results. In addition, damping coefficient is even higher, as evidenced by the rapid, almost immediate damping of the oscillatory motion. Similar to the mechanical setup, the absorber never returns to the sag point however deviation is even greater.

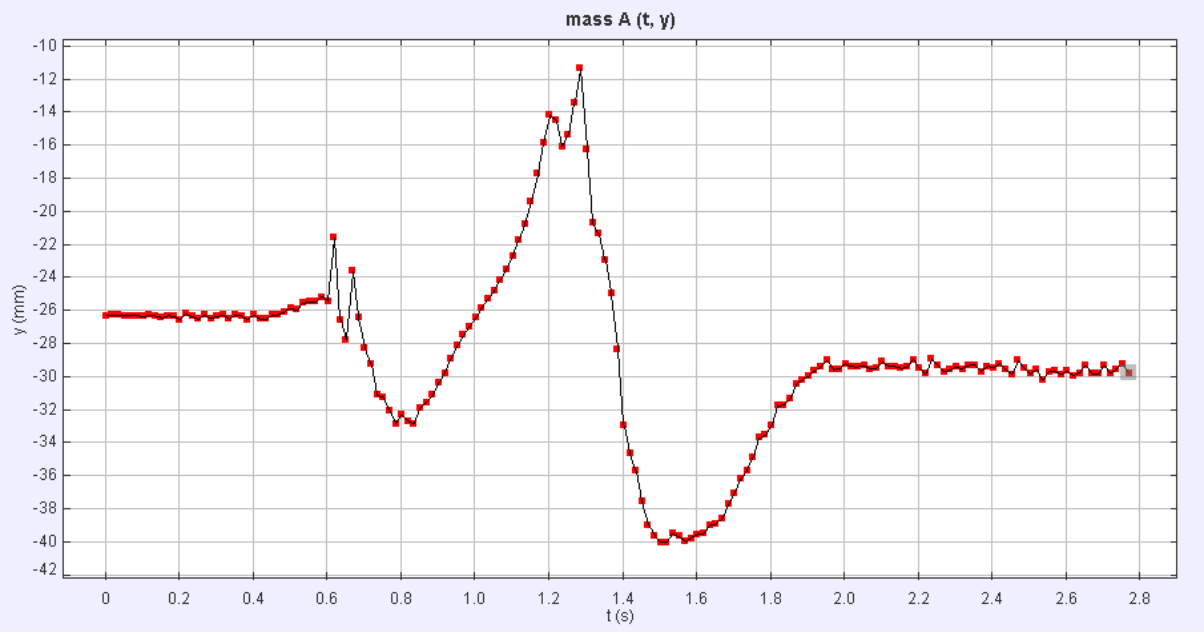

Figure 35: Electrical Damping Results

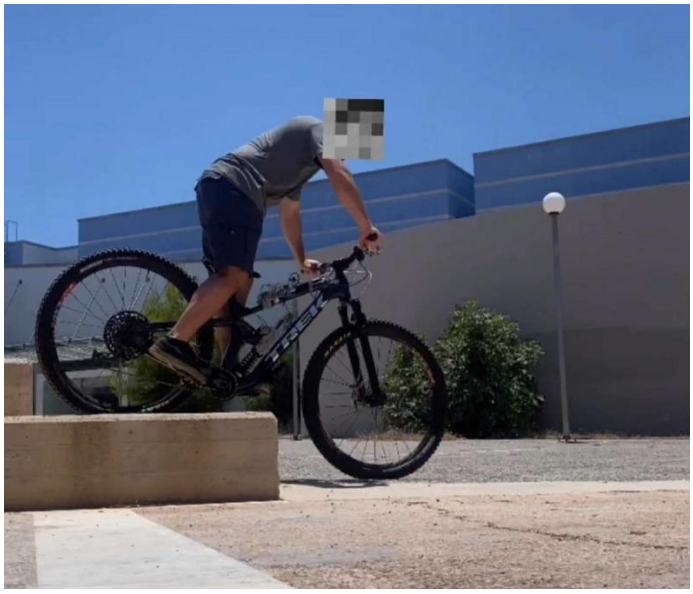

Figure 36: Execution of the step-drop experiment.

5.2.2 Calculation of Generated Voltage and Power

The following diagrams present the voltage response recorded during the drop test. In Fig. 37, the initial transient corresponds to the rider boarding on the bicycle and initiating pedaling, which generates approximately 6 V (≈6 W). After this phase, the signal remains stable until the front wheel descends from the step and contacts the ground, producing three distinct spikes, the largest of which reaches 23 V (≈18 W). This impact causes compression of the rear suspension, which in turn produces a higher voltage spike as the rear wheel strikes the ground, reaching 33 V (≈42 W). A subsequent, smaller peak can be attributed to the damping process as oscillations decay, while the final two transients are associated with the rider stepping off the bicycle.

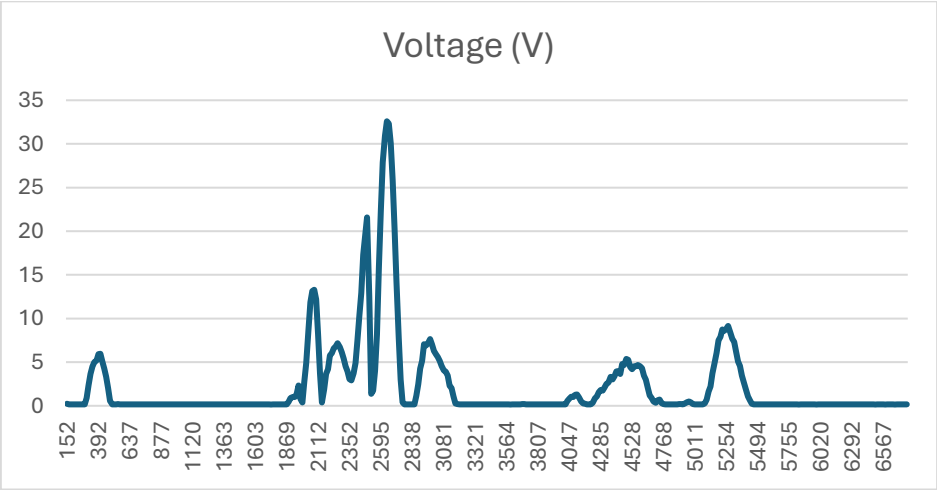

Figure 37: Generated voltage (V/ms)

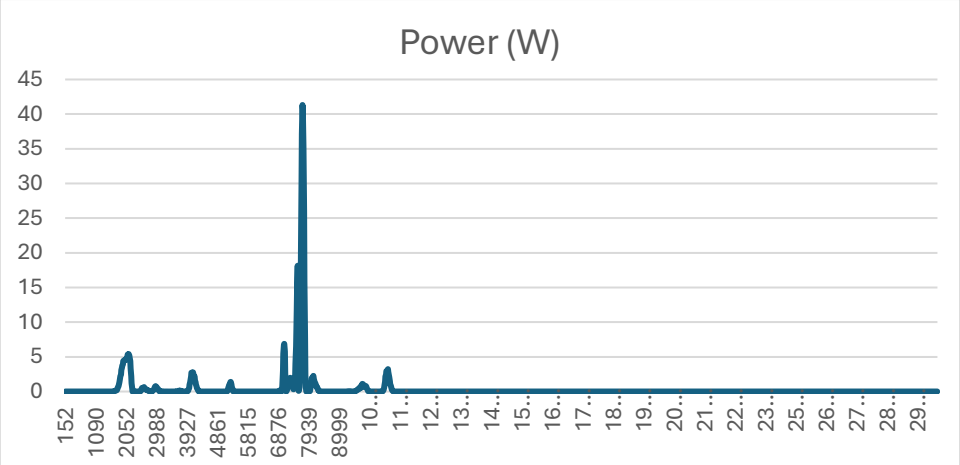

Figure 38: Power generated from the circuit (W/ms)

5.3 Results and Discussion

To provide a final validation of the RSA's operational performance, a field test was conducted on the university campus. The experiment was recorded using GPS tracking, and the corresponding route visualization is presented in Fig. 39. The ride lasted 8 minutes and 30 seconds, covering a total distance of 2.76 km with an elevation gain of 32 m. During the ride, the absorber generated 0.27 Watt. With regard to road classification, the test surface cannot be categorized as class E, which generally represents rough, unpaved terrain. Rather, it corresponds more closely to class B conditions, as the pavement consisted of asphalt with minor surface irregularities.

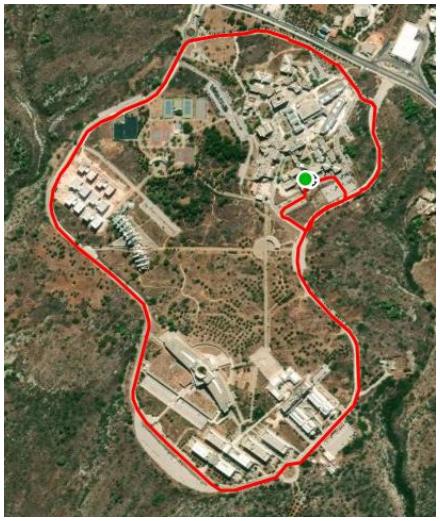

Figure 39: GPS-tracked test route on university campus

6. Conclusions and Future Work

6.1 Summary of Findings

This thesis proposes an effective way to utilize the dissipating energy which is produced through the movement of the suspension system of an enduro E-bicycle, while riding. Initially, simulations of bicycle motion on a class-E road were performed to obtain data on the forces and velocities acting on the linkage, which allowed for the prediction of the voltage produced by the suspension system. As described in Chapter 3.1, the first step involved the 3D modeling of the Trek Slash Gen 5, which was subsequently implemented in ANSYS. To refine the model, experimental data from motion video analysis, presented in Chapter 3.2, were also incorporated. The simulation process, completed in Chapter 3.3, was supported by MATLAB, which was used both to generate the road profile inserted in ANSYS environment and to simulate the corresponding electrical circuit, predicting the voltage output.

Following the completion of the simulations, the construction of the regenerative shock absorber was undertaken. Chapter 4.1 outlines the design methodology, including the definition of constraints and the selection of components based on the ANSYS analysis presented in Chapter 3, in order to achieve the desired performance. Chapters 4.2 and 4.3 describe the operation of the mechanism, the electrical circuit, and the Arduino control system. The final subchapter details the practical construction of the absorber and the manufacturing process followed.

The final stage of this thesis involved experimental validation. As described in Chapter 5.1, the RSA was mounted on the bicycle, and two experiments were conducted, differing only in the inclusion of the electrical circuit. In the mechanical case, the circuit was not engaged, whereas in the second test the complete system was evaluated. The output of the second experiment was the voltage and power generated by the absorber, which were subsequently compared with the ANSYS simulation results. The comparison demonstrated that the experimental and simulated graphs were nearly identical, confirming the accuracy of the model. As presented in Chapter 5.3, the absorber produced approximately 0.27-Watt average during an 8.5-minute ride covering 2.7 km, in a road class-B.

The analysis demonstrates that under smooth road conditions (Class B), the regenerative suspension system produces 5.72 Wh of energy over a three-hour period. For a standard 625 Wh e-MTB battery, this represents a marginal charge of approximately 1%. On a rough road profile (Class E), the energy yield is projected to increase by a factor of 4 to 10 [33].

This results in an average energy harvest of 28.6 Wh, corresponding to a more substantial 5% increase in the battery's State of Charge (SoC). In practical terms, this

allows a rider to extend their range by an estimated 4 to 5 kilometers under typical trail conditions. This level of autonomous energy generation constitutes a significant enhancement to the vehicle's operational endurance, providing a tangible improvement in rider security and range confidence.

6.2 Future Work

Future work should focus on improving data acquisition, refining the dynamic model, and optimizing absorber properties with a PID controller. Design improvements include reducing the absorber's weight to limit its impact on the bicycle mass and redesigning the main body to correct shortcomings from the first prototype. Finally, validation on a Class E Road would provide practical confirmation of the concept's effectiveness.

References

[1] J. Cui, W. Y. Szeto, and Y. Wang, "A static mixed bike repositioning problem with both man-powered bikes and e-bikes," *Transportation Research Part E: Logistics and Transportation Review*, vol. 203, p. 104275, Nov. 2025, doi: 10.1016/j.tre.2025.104275.

[2] P. Zheng, J. Gao, R. Wang, J. Dong, and J. Diao, "Review on the Research of Regenerative Shock Absorber," in *2018 24th International Conference on Automation and Computing (ICAC)*, Newcastle upon Tyne, United Kingdom: IEEE, Sept. 2018, pp. 1–12. doi: 10.23919/IConAC.2018.8749044.

[3] N. Hannan, S. K. Shib, A. Shufian, M. A. Islam, S. M. Islam Sharan, and A. D. Gupta, "Advanced regenerative braking system for EVs: Leveraging BLDC-supercapacitor technologies for optimized energy recovery, economic viability, and maintenance strategies," *Future Batteries*, vol. 7, p. 100103, Sept. 2025, doi: 10.1016/j.fub.2025.100103.

[4] Y. Koda, H. Osawa, N. Nagatsuka, S. Kariya, T. Inagawa, and K. Ishizuka, "Development of Bidirectional Series Elastic Actuator with Torsion Coil Spring and Implementation to the Legged Robot," in *2024 IEEE/RSJ International Conference on Intelligent Robots and Systems (IROS)*, Abu Dhabi, United Arab Emirates: IEEE, Oct. 2024, pp. 9082–9087. doi: 10.1109/IROS58592.2024.10802064.

[5] N. T. Cong and P. D. Binh, "Simulation and Investigation of the Influence of Pressure on the Stiffness of Air Spring Suspension in Passenger Vehicles Using ABAQUS," in *Proceedings of the 3rd Annual International Conference on Material, Machines and Methods for Sustainable Development (MMMS2022)*, B. T. Long, K. Ishizaki, H. S. Kim, Y.-H. Kim, N. D. Toan, N. T. H. Minh, and P. Duc An, Eds., in Lecture Notes in Mechanical Engineering. , Cham: Springer Nature Switzerland, 2024, pp. 155–161. doi: 10.1007/978-3-031-57460-3_17.

[6] S. Wulandari, B. H. Iswanto, and I. Sugihartono, "Determination of Springs Constant by Hooke's Law and Simple Harmonic Motion Experiment," *J. Phys.: Conf. Ser.*, vol. 2019, no. 1, p. 012053, Oct. 2021, doi: 10.1088/1742-6596/2019/1/012053.

[7] S. Breitenbach, M. Skoglund, J. Lillepärg, T. Emmler, and F. Mantwill, “On the influence of sorbents on the static stiffness of Air Springs,” *Forsch Ingenieurwes*, vol. 88, no. 1, p. 32, Dec. 2024, doi: 10.1007/s10010-024-00752-4.

[8] M. B. Gerrard, “Kinematic Suspension Linkages - A Model for Their Behaviour and a Procedure for Their Design,” presented at the SAE 2002 World Congress & Exhibition, Mar. 2002, pp. 2002-01–0281. doi: 10.4271/2002-01-0281.

[9] A. Tempia, A. Subic, and R. M. Pagliarella, “Dynamic Characteristics of Modern Mountain Bikes Rear Linkages,” in *The Engineering of Sport 6*, E. F. Moritz and S. Haake, Eds., New York, NY: Springer New York, 2006, pp. 91–96. doi: 10.1007/978-0-387-46050-5_17.

[10] S. A. Needle and M. L. Hull, “An Off-Road Bicycle With Adjustable Suspension Kinematics,” *Journal of Mechanical Design*, vol. 119, no. 3, pp. 370–375, Sept. 1997, doi: 10.1115/1.2826357.

[11] J. Gao and P. Han, “Analysis and Optimization of Suspension Spring Stiffness for Improving Frequency Response Characteristics of the Vehicle,” *Mathematical Problems in Engineering*, vol. 2022, pp. 1–19, May 2022, doi: 10.1155/2022/9557483.

[12] K. J. Kadhim, “Experimental investigation of the effect of damping coefficients on spring diameter thickness,” *Journal of Achievements in Materials and Manufacturing Engineering*, vol. 115, no. 1, pp. 16–25, Nov. 2022, doi: 10.5604/01.3001.0016.2338.

[13] A. B. Abdelwahed, J. Chakhari, and C. Mrad, “Effect of Valves Stiffness on the Performance of a Twin-Tube Hydraulic Damper,” *WSEAS TRANSACTIONS ON APPLIED AND THEORETICAL MECHANICS*, vol. 19, pp. 143–155, Jan. 2025, doi: 10.37394/232011.2024.19.16.

[14] X. D. Xie and Q. Wang, “Energy harvesting from a vehicle suspension system,” *Energy*, vol. 86, pp. 385–392, June 2015, doi: 10.1016/j.energy.2015.04.009.

[15] X. D. Xie and Q. Wang, “Energy harvesting from a vehicle suspension system,” *Energy*, vol. 86, pp. 385–392, June 2015, doi: 10.1016/j.energy.2015.04.009.

[16] P. Li and L. Zuo, “Influences of the electromagnetic regenerative dampers on the vehicle suspension performance,” *Proceedings of the Institution of Mechanical Engineers, Part D: Journal of Automobile Engineering*, vol. 231, no. 3, pp. 383–394, Feb. 2017, doi: 10.1177/0954407016639503.

[17] S. Guo, L. Xu, Y. Liu, X. Guo, and L. Zuo, “Modeling and Experiments of a Hydraulic Electromagnetic Energy-Harvesting Shock Absorber,” *IEEE/ASME Trans. Mechatron.*, vol. 22, no. 6, pp. 2684–2694, Dec. 2017, doi: 10.1109/TMECH.2017.2760341.

[18] P. Pan, D. Zhang, X. Nie, and H. Chen, “Development of piezoelectric energy-harvesting tuned mass damper,” *Sci. China Technol. Sci.*, vol. 60, no. 3, pp. 467–478, Mar. 2017, doi: 10.1007/s11431-016-0280-5.

[19] W. M. Saslow, “Faraday’s Law of Electromagnetic Induction,” in *Electricity, Magnetism, and Light*, Elsevier, 2002, pp. 505–558. doi: 10.1016/B978-012619455-5.50012-7.

[20] J. Høgsberg, “Tuning of a Viscous Inerter Damper: How to Achieve Resonant Damping Without a Damper Resonance,” *Applied Sciences*, vol. 15, no. 2, p. 676, Jan. 2025, doi: 10.3390/app15020676.

[21] W. J. Song, B. Y. Moon, J. Kim, and B. S. Kang, “Experimental Study on Mechanical Damping System Using Colloid Suspension,” *KEM*, vol. 274–276, pp. 775–780, Oct. 2004, doi: 10.4028/www.scientific.net/KEM.274-276.775.

[22] P. Li and L. Zuo, “Influences of the electromagnetic regenerative dampers on the vehicle suspension performance,” *Proceedings of the Institution of Mechanical Engineers, Part D: Journal of Automobile Engineering*, vol. 231, no. 3, pp. 383–394, Feb. 2017, doi: 10.1177/0954407016639503.

[23] W. Wang and S. Liu, “Control and Simulation of Regenerative Suspension Using Permanent Magnetic Synchronous Motor,” in *Proceedings of the FISITA 2012 World Automotive Congress*, vol. 195, SAE-China and FISITA, Eds., in Lecture Notes in Electrical Engineering, vol. 195. , Berlin, Heidelberg: Springer Berlin Heidelberg, 2013, pp. 505–514. doi: 10.1007/978-3-642-33835-9_46.

[24] Y. Okada, H. Harada, and K. Suzuki, “Active and Regenerative Control of an Electrodynamic-Type Suspension.,” *JSME Int. J., Ser. C*, vol. 40, no. 2, pp. 272–278, 1997, doi: 10.1299/jsmec.40.272.

[25] Y. Kawamoto, Y. Suda, H. Inoue, and T. Kondo, “Modeling of Electromagnetic Damper for Automobile Suspension,” *JSDD*, vol. 1, no. 3, pp. 524–535, 2007, doi: 10.1299/jsdd.1.524.

[26] Y. Cui, M. Faizan, and Z. Chen, “Back EMF Waveform Comparison and Analysis of Two Kinds of Electrical Machines,” *WEVJ*, vol. 12, no. 3, p. 149, Sept. 2021, doi: 10.3390/wevj12030149.

[27] Z. Jia, Y. Liu, Y. Shen, C. Luo, and X. Yang, “Performance Analysis of Vehicle EM–ISD Suspension Considering Parasitic Damping,” *Machines*, vol. 13, no. 8, p. 690, Aug. 2025, doi: 10.3390/machines13080690.

[28] M. C. Smith and S. J. Swift, “Design of passive vehicle suspensions for maximal least damping ratio,” *Vehicle System Dynamics*, vol. 54, no. 5, pp. 568–584, May 2016, doi: 10.1080/00423114.2016.1145242.

[29] J. A. Little and B. P. Mann, “Optimizing logarithmic decrement damping estimation through uncertainty propagation,” *Journal of Sound and Vibration*, vol. 457, pp. 368–376, Sept. 2019, doi: 10.1016/j.jsv.2019.05.040.

[30] S. Li, J. Xu, X. Pu, T. Tao, H. Gao, and X. Mei, “Energy-harvesting variable/constant damping suspension system with motor based electromagnetic damper,” *Energy*, vol. 189, p. 116199, Dec. 2019, doi: 10.1016/j.energy.2019.116199.

[31] T. Shukla, “An isolated asymmetrical AC-DC converter based brushless direct current motor drive without bridge rectifier and low pass filter,” *e-Prime - Advances in Electrical Engineering, Electronics and Energy*, vol. 12, p. 100998, June 2025, doi: 10.1016/j.prime.2025.100998.

[32] A. P. Mudrov, R. I. Siraev, F. F. Khabibullin, R. T. Islamov, M. R. Faizov, and T. A. Mustafaev, “Braking force influence on mountain bike suspension,” *J. Phys.: Conf. Ser.*, vol. 2373, no. 9, p. 092001, Dec. 2022, doi: 10.1088/1742-6596/2373/9/092001.

[33]

L. Qi, J. Song, Y. Wang, M. Yi, Z. Zhang, and J. Yan, “Mechanical motion rectification-based electromagnetic vibration energy harvesting technology: A review,” *Energy*, vol. 289, p. 130030, Feb. 2024, doi: 10.1016/j.energy.2023.130030.

Appendices

Detailed CAD Drawings.

Parts List

Item	Qty	Part Number	Material
1	1	Rack	Steel
2	1	Spur gear	Steel
3	1	Frame	----
4	1	Guide rack	Steel
5	1	Body2	Steel
6	4	BB spacer	Steel
7	1	Rack base	Steel
8	4	4648K307_Permanently Lubricated Stainless Steel Ball Bearing	Steel
9	4	Component24	Steel
10	1	Motor assembly v1	Steel
11	4	91290A168_Alloy Steel Socket Head Screw	Steel
12	4	Component31	Steel
13	3	Component32	Steel
14	3	94645A205_High-Strength Steel Nylon-Insert Locknut	Steel
15	3	91310A128_High-Strength Class 10.9 Steel Hex Head Screw	Steel
16	2	94645A102_High-Strength Steel Nylon-Insert Locknut	Steel
17	2	91310A124_High-Strength Class 10.9 Steel Hex Head Screw	Steel
18	2	Component38	Steel
19	1	4668K225_Permanently Lubricated Stainless Steel Ball Bearing	Steel
20	1	91290A242_Alloy Steel Socket Head Screw	Steel

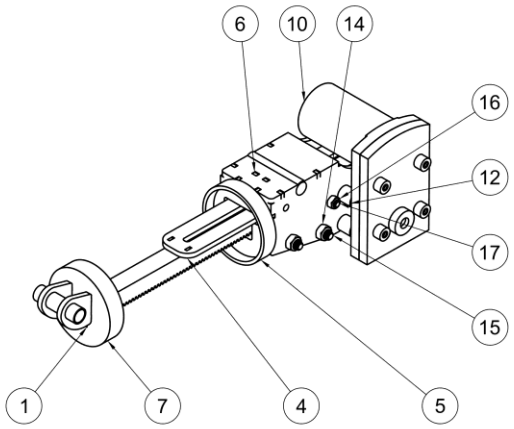

Dept.	Technical reference	Created by: Dimitris Moumougiannis 19/09/2025	Approved by
		Document type	Document status
		Title: Assem1	DWG No.
		Rev.	Date of issue / Sheet: 1/18

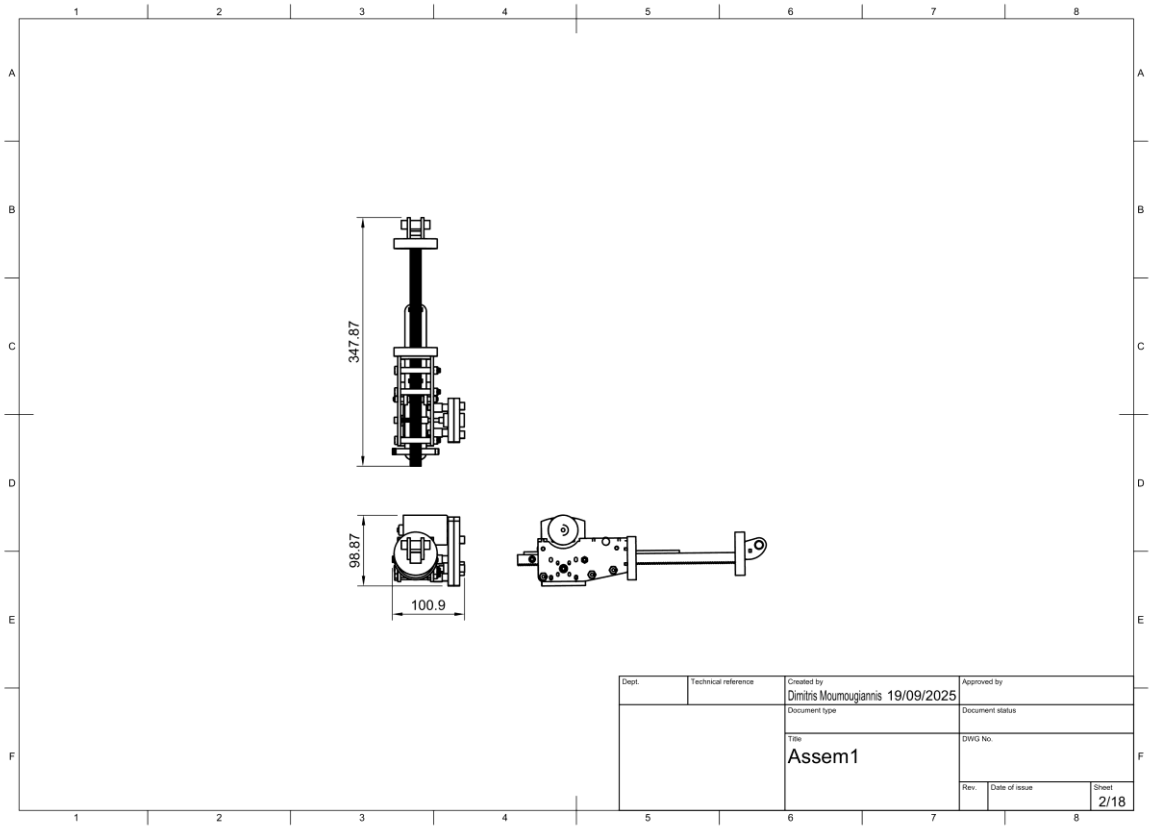

Dept.	Technical reference	Created by: Dimitris Moumougiannis 19/09/2025	Approved by
		Document type	Document status
		Title: Assem1	DWG No.
			Rev. / Date of issue / Sheet: 2/18

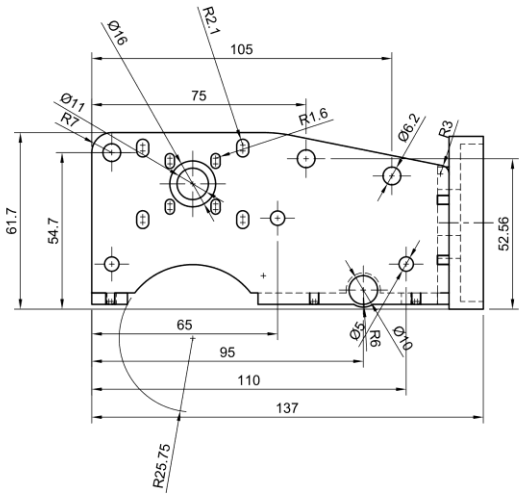

Dept.	Technical reference	Created by: Dimitris Moumougiannis 19/09/2025	Approved by
		Document type	Document status
		Title: Assem1	DWG No.
			Rev. / Date of issue / Sheet: 6/18

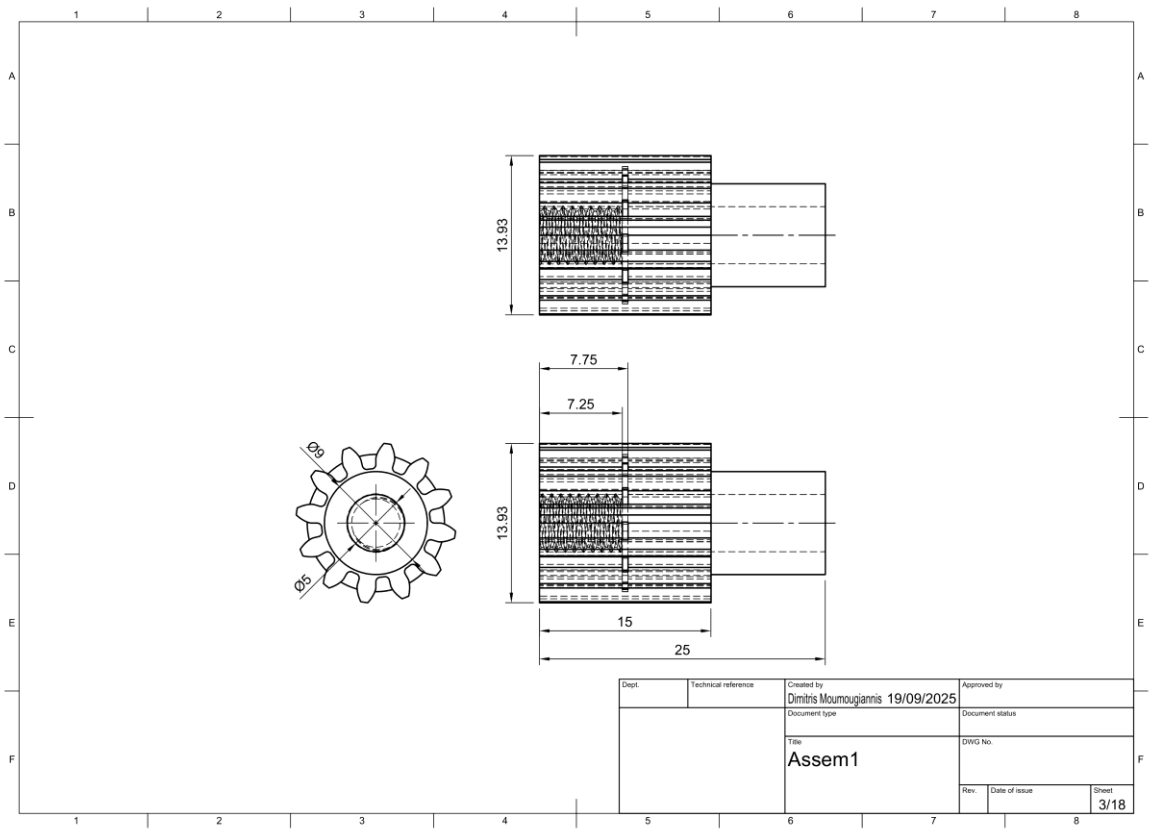

Dept.	Technical reference	Created by Dimitris Moumougiannis 19/09/2025	Approved by
		Document type	Document status
		Title: Assem1	DWG No.
			Rev. / Date of issue / Sheet: 3/18

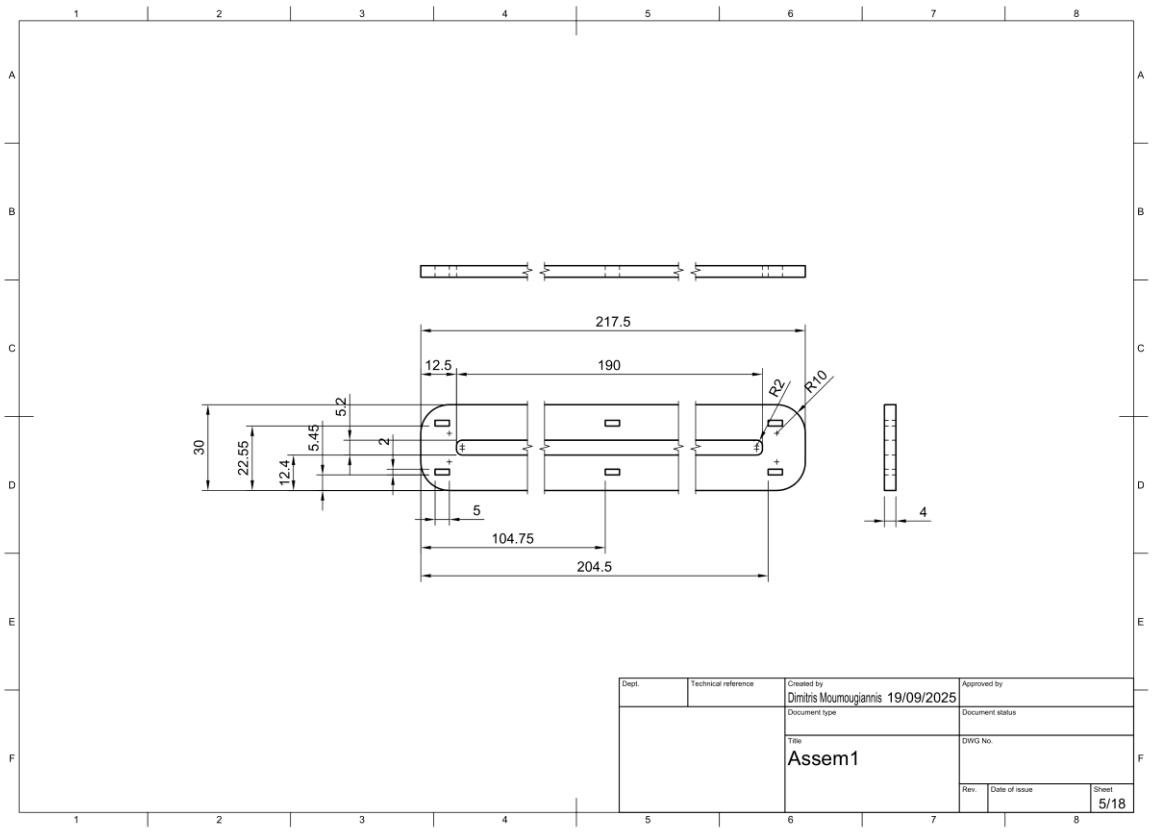

Dept.	Technical reference	Created by Dimitris Moumougiannis 19/09/2025	Approved by
		Document type	Document status
		Title: Assem1	DWG No.
			Rev. / Date of issue / Sheet: 5/18

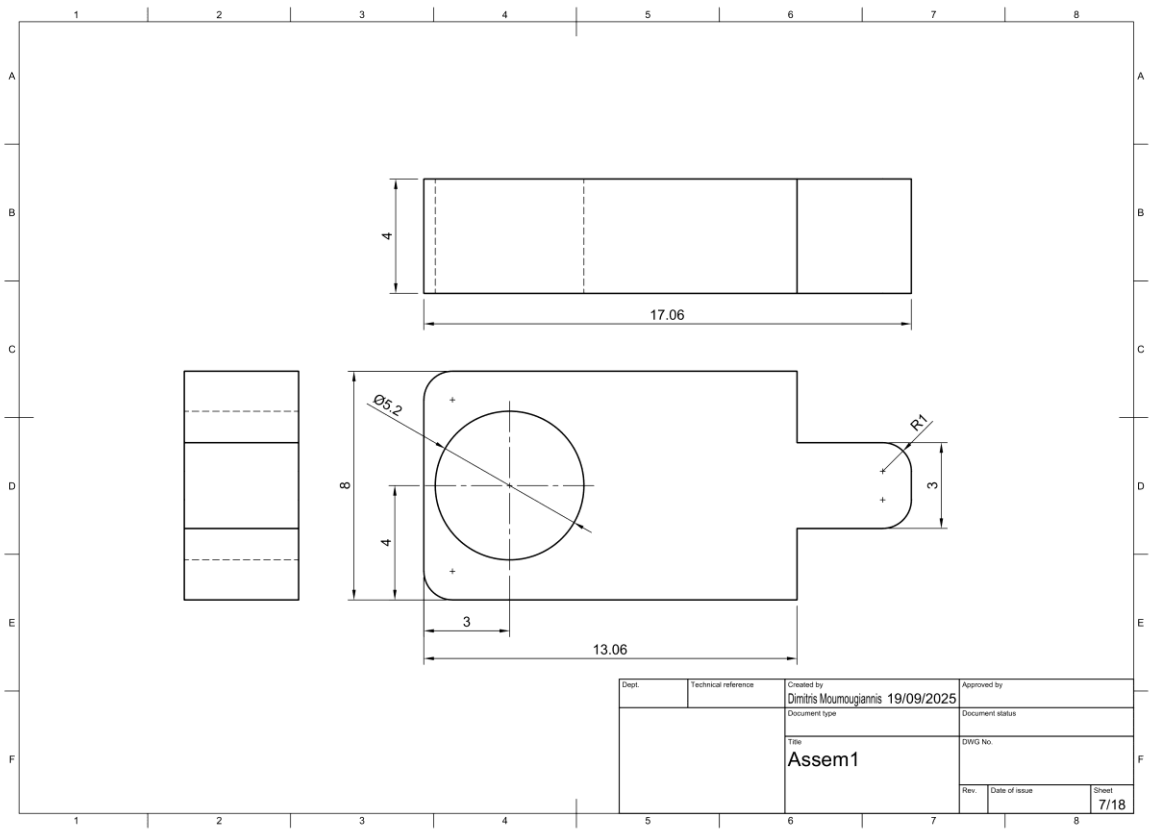
4
17.06
Ø5.2
R1
8
4
3
3
13.06
Dept.
Technical reference
Created by
Dimitris Moumougiannis 19/09/2025
Approved by
Document type
Document status
Title
Assem1
DWG No.
Rev.
Date of issue
Sheet
7/18

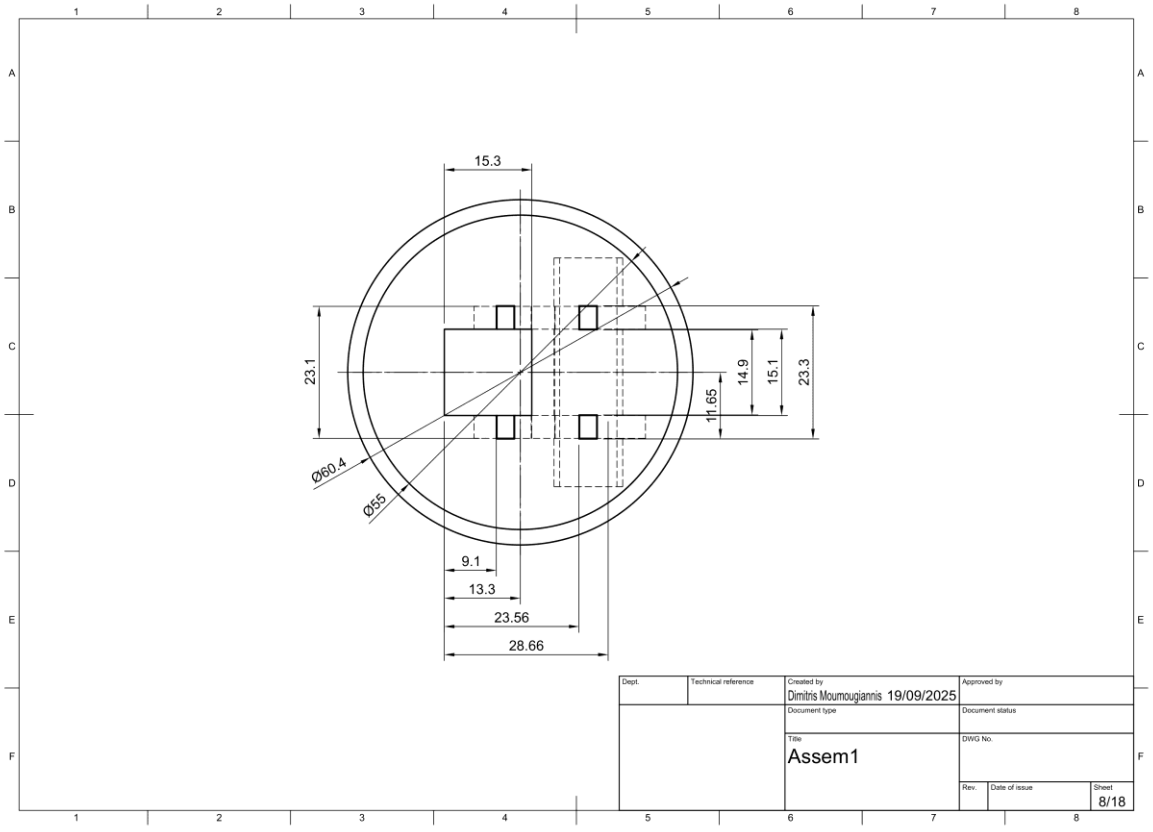
15.3
23.1
14.9
15.1
23.3
11.65
Ø60.4
Ø55
9.1
13.3
23.56
28.66
Dept.
Technical reference
Created by
Dimitris Moumougiannis 19/09/2025
Approved by
Document type
Document status
Title
Assem1
DWG No.
Rev.
Date of issue
Sheet
8/18

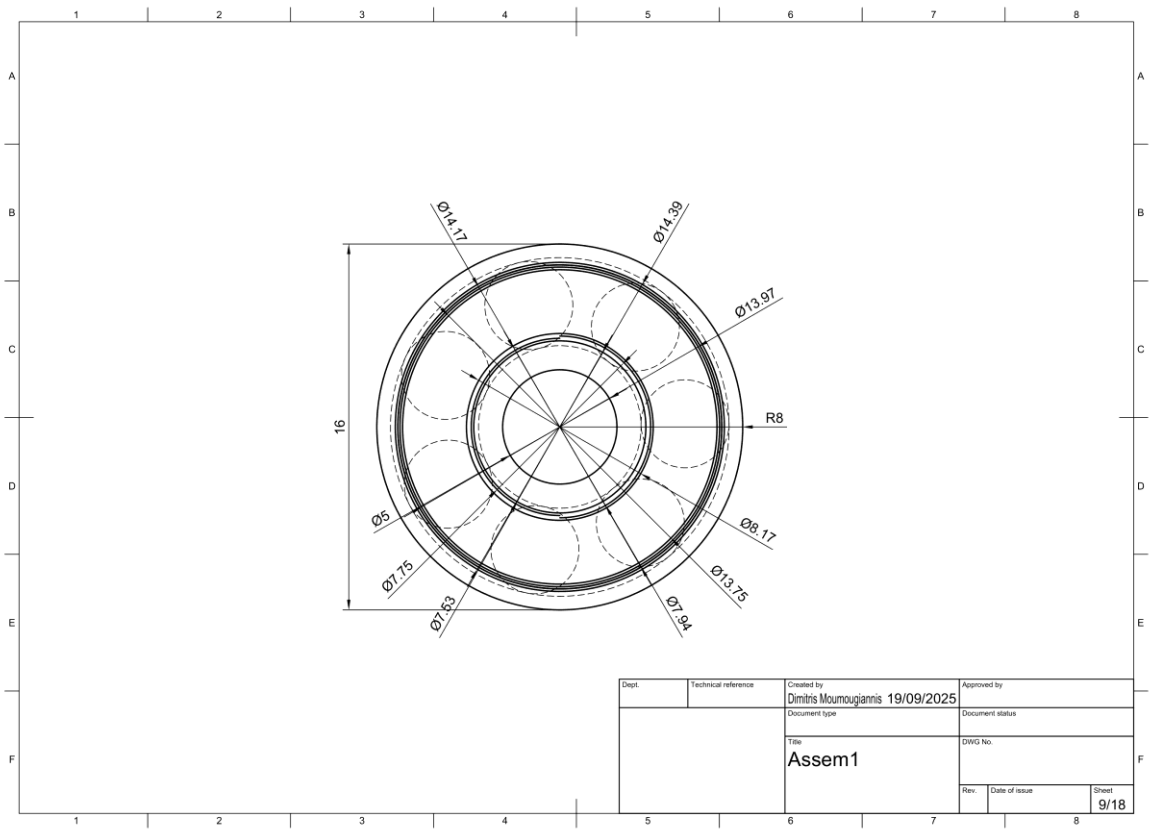

Dept.	Technical reference	Created by Dimitris Moumougiannis 19/09/2025	Approved by
		Document type	Document status
		Title: Assem1	DWG No.
			Rev. / Date of issue / Sheet 9/18

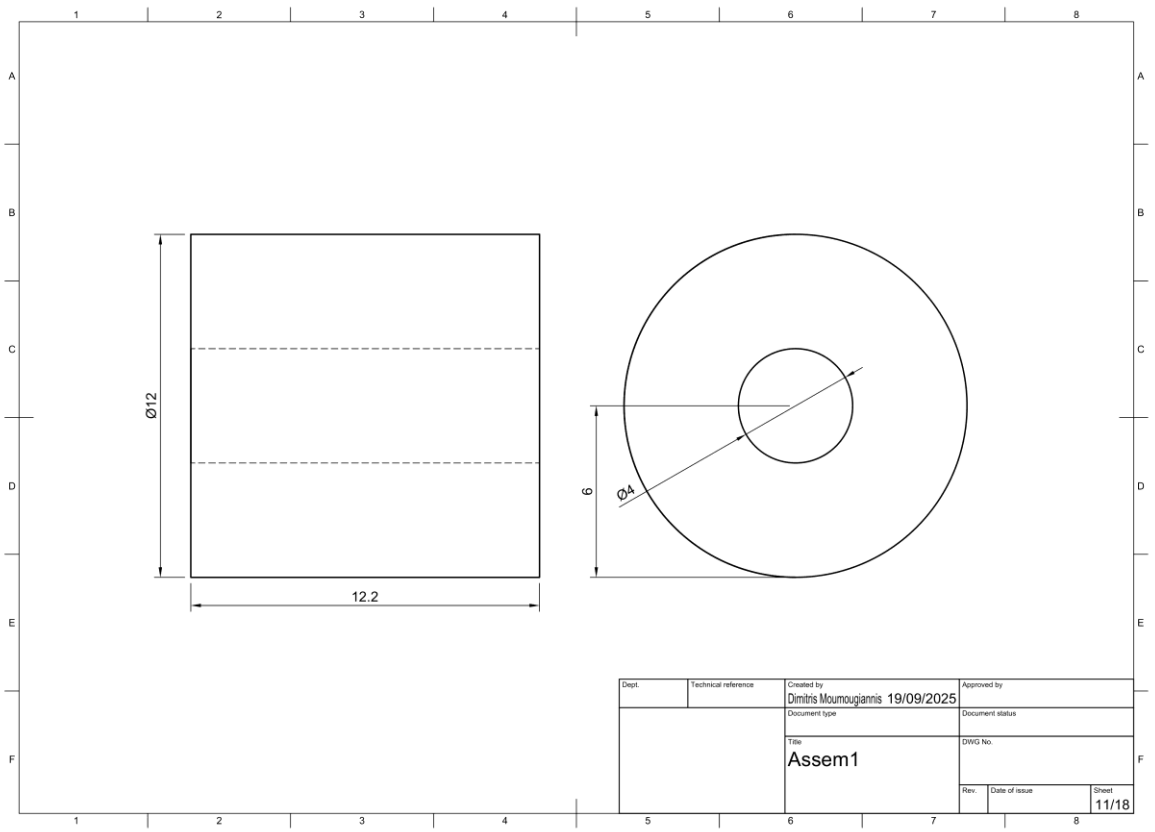
Ø12
12.2
9
Ø4
Dept.
Technical reference
Created by
Dimitris Moumougiannis 19/09/2025
Approved by
Document type
Document status
Title
Assem1
DWG No.
Rev.
Date of issue
Sheet
11/18

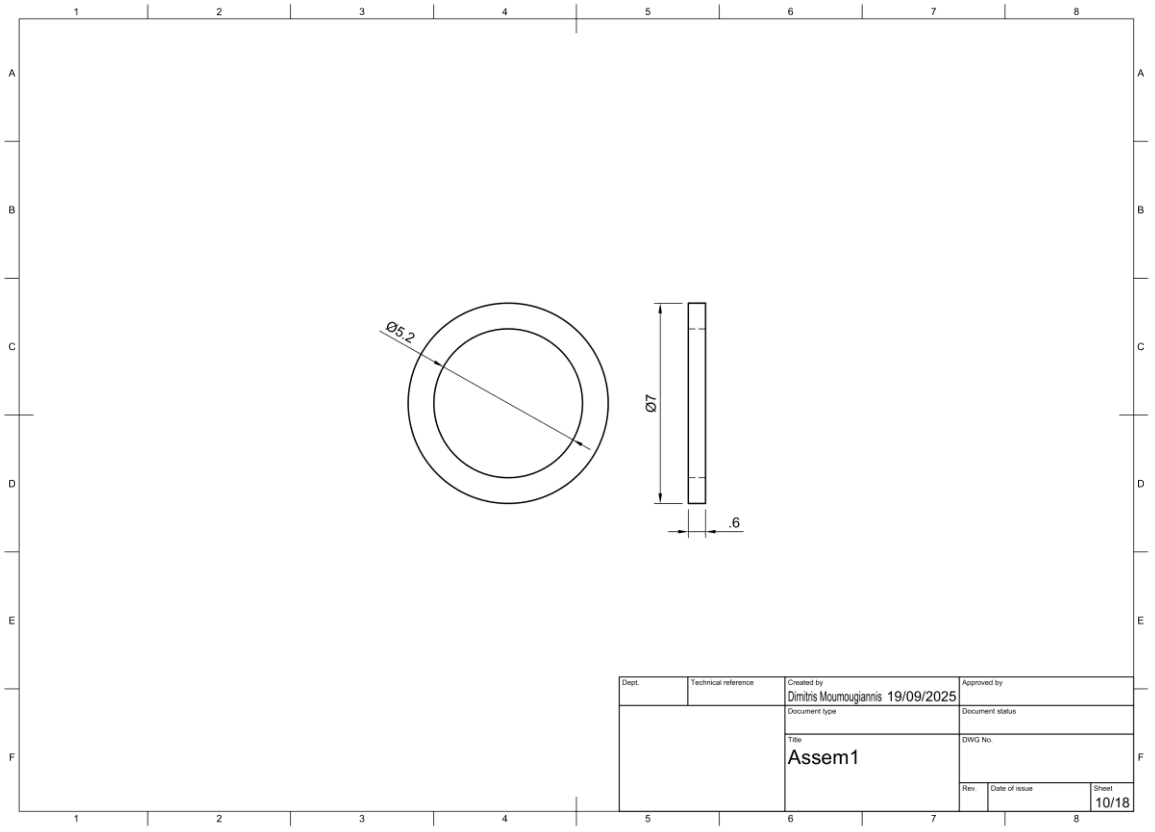
Ø5.2
Ø7
.6
Dept.
Technical reference
Created by
Dimitris Moumougiannis 19/09/2025
Approved by
Document type
Document status
Title
Assem1
DWG No.
Rev.
Date of issue
Sheet
10/18

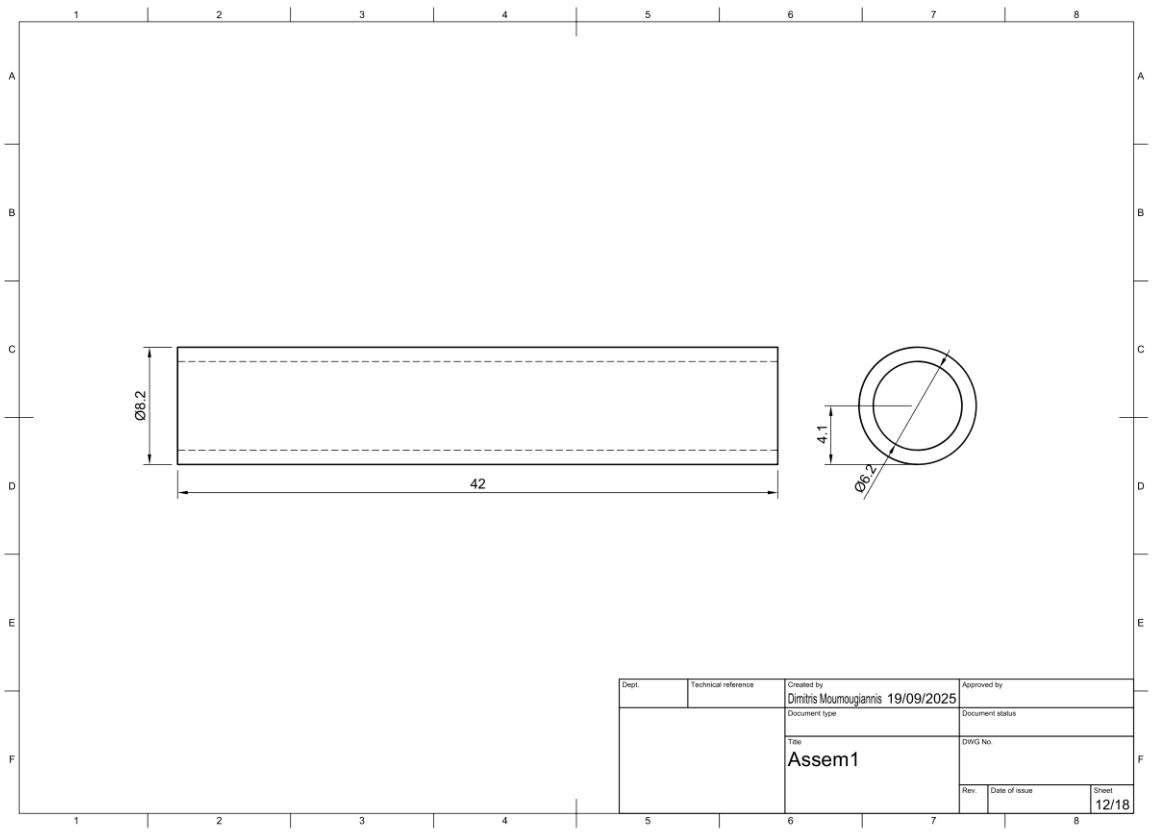
Ø8.2
42
4.1
Ø6.2
Dept.
Technical reference
Created by
Dimitris Moumougiannis 19/09/2025
Approved by
Document type
Document status
Title
Assem1
DWG No.
Rev.
Date of issue
Sheet
12/18

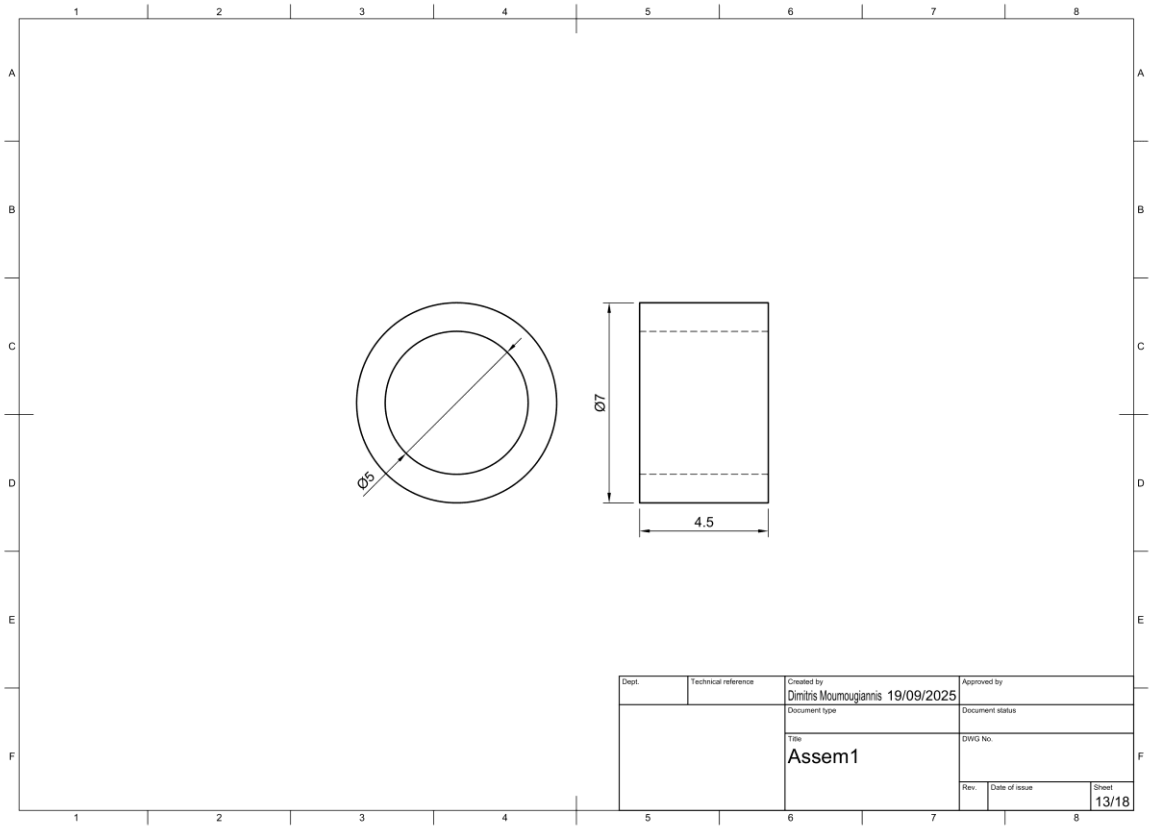
Ø5
Ø7
4.5
Dept.
Technical reference
Created by
Dimitris Moumougiannis 19/09/2025
Approved by
Document type
Document status
Title
Assem1
DWG No.
Rev.
Date of issue
Sheet
13/18

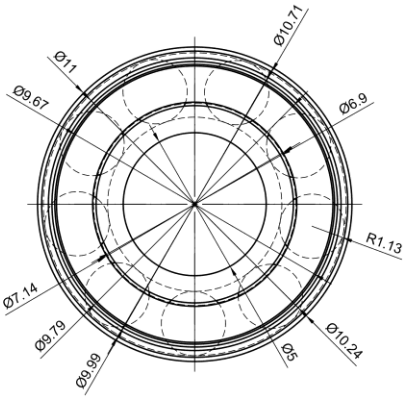

Dept.	Technical reference	Created by: Dimitris Moumougiannis 19/09/2025	Approved by
		Document type	Document status
		Title: Assem1	DWG No.
			Rev. / Date of issue / Sheet: 14/18

Parts List			
Item	Qty	Part Number	Material
1	2	Component39	Steel
2	1	94645A102_High-Strength Steel Nylon-Insert Locknut	Steel
3	1	91290A199_Alloy Steel Socket Head Screw	Steel

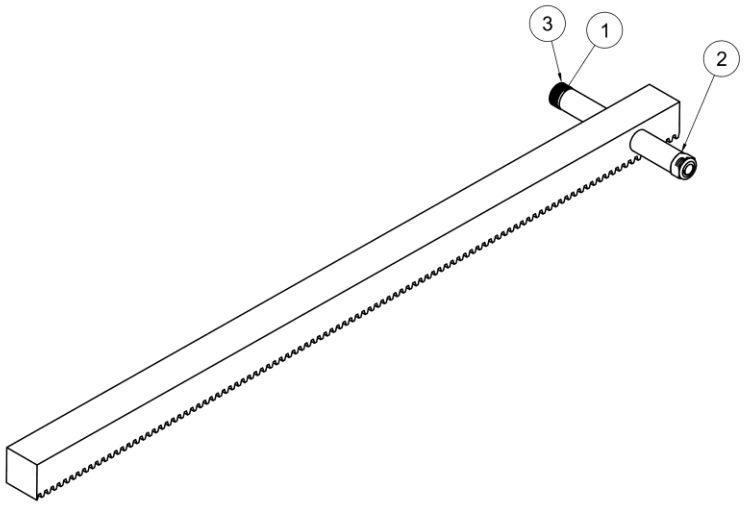

Dept.	Technical reference	Created by: Dimitris Moumougiannis 19/09/2025	Approved by
		Document type	Document status
		Title: Assem1	DWG No.
			Rev. / Date of issue / Sheet: 15/18

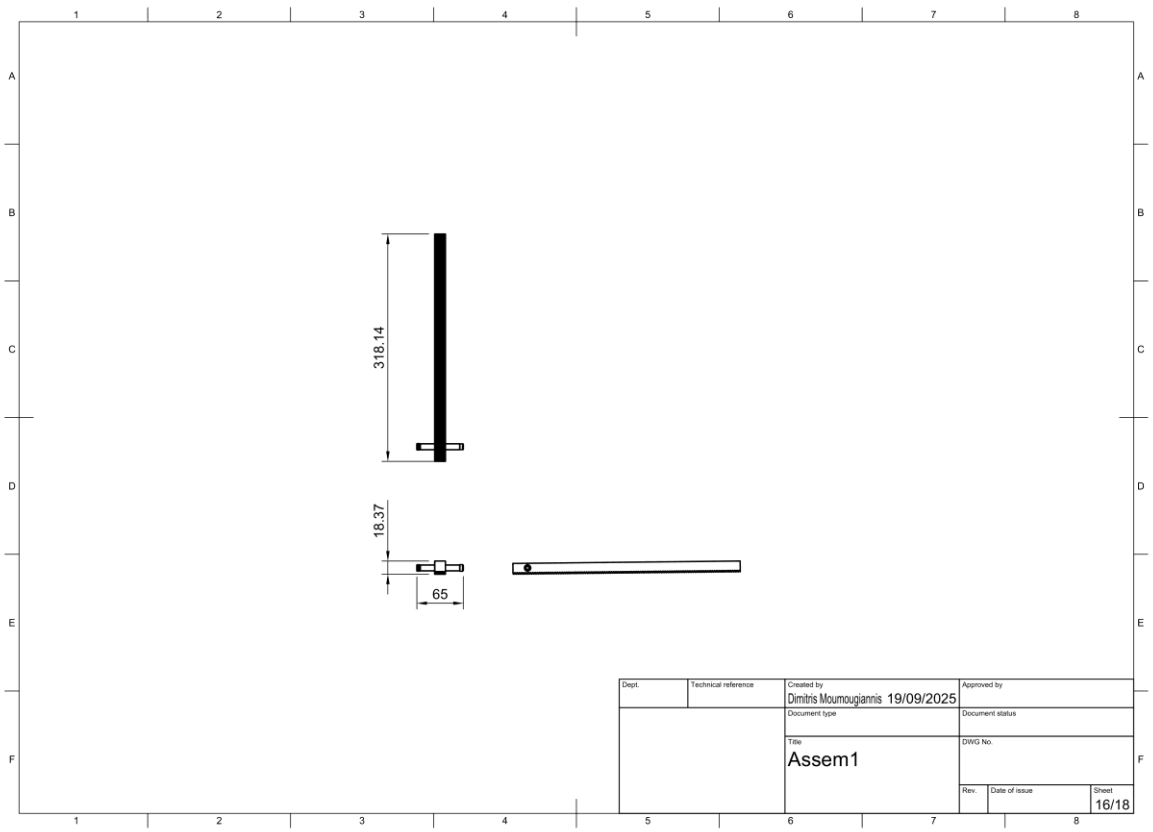

Dept.	Technical reference	Created by: Dimitris Moumougiannis 19/09/2025	Approved by
		Document type	Document status
		Title: Assem1	DWG No.
			Rev. / Date of issue / Sheet: 16/18

Parts List			
Item	Qty	Part Number	Material
1	1	Motor 24v v2	Steel
2	1	GEARBOX v12	Steel

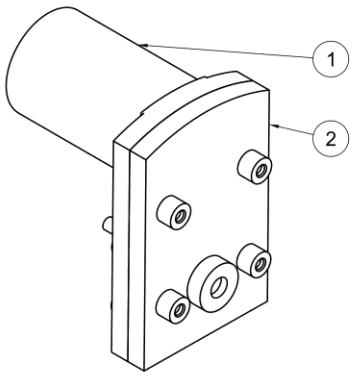

Dept.	Technical reference	Created by: Dimitris Moumougiannis 19/09/2025	Approved by
		Document type	Document status
		Title: Assem1	DWG No.
			Rev. / Date of issue / Sheet: 17/18

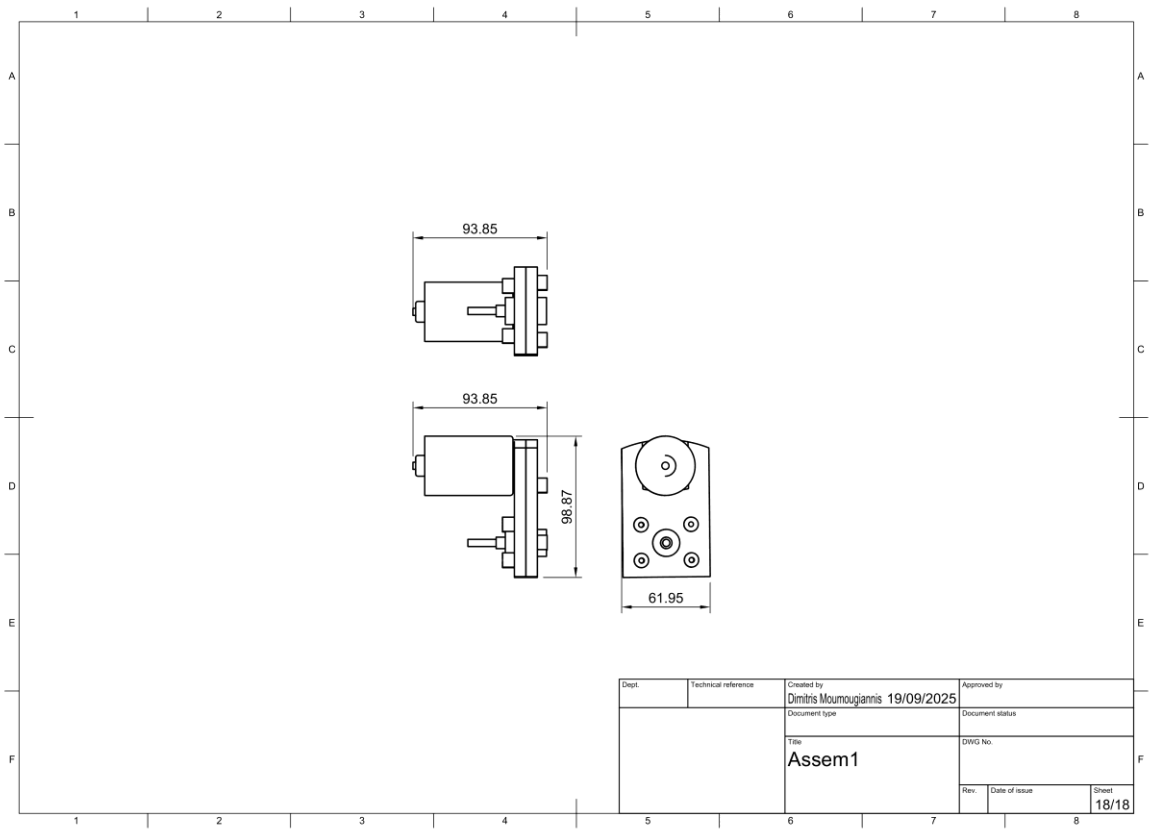

Arduino Code

```
#include <Wire.h>

#include <Adafruit_INA219.h>

#include <SPI.h> // Required for SD Card communication

#include <SD.h>  // SD Card library


Adafruit_INA219 ina219; // Create an object for the INA219 sensor


// --- SD CARD SETTINGS ---

const int chipSelect = 10; // Chip Select (CS) pin for the SD card module. Typically pin 10.


// --- GLOBAL VARIABLE FOR FILENAME ---

// This variable stores the filename (e.g., "LOG00.CSV").
```

```
// It is "global" to be accessible in all functions (setup, loop).
char filename[13];

// --- RECORDING DURATION SETTINGS ---
// The duration of the experiment in milliseconds.
const unsigned long RECORDING_WINDOW_DURATION_MS = 15000; // 15 seconds

// --- SAMPLING FREQUENCY SETTING ---
// The interval in milliseconds between each sample.
// 8 ms means ~125 samples/second (~125 fps).
const unsigned long SAMPLING_INTERVAL_MS = 8;

// --- LED FOR VISUAL INDICATION ---
// We use the Arduino's built-in LED (usually pin 13).
const int LED_PIN = LED_BUILTIN;

// --- TIMING AND RECORDING VARIABLES ---
unsigned long recordingStartTime = 0;
bool isRecording = false; // Flag: true if we are recording, false otherwise
int currentSampleCount = 0; // Counter for the number of samples written

File dataFile; // Global File object for SD card operations

void setup() {
  Serial.begin(9600);
  Wire.begin();
  pinMode(LED_PIN, OUTPUT);

  // --- Startup Indication & SD Card Check ---
  // The LED blinks 2 times to show the Arduino is starting.
```

```
digitalWrite(LED_PIN, HIGH); delay(200);
digitalWrite(LED_PIN, LOW);  delay(200);
digitalWrite(LED_PIN, HIGH); delay(200);
digitalWrite(LED_PIN, LOW);  delay(200);

Serial.print("Initializing SD card...");
// Try to initialize the SD card.
if (!SD.begin(chipSelect)) {
  Serial.println("SD card initialization failed! Check connections or card.");
  // If it fails, the LED blinks rapidly continuously (critical error).
  while (true) {
    digitalWrite(LED_PIN, HIGH); delay(100);
    digitalWrite(LED_PIN, LOW);  delay(100);
  }
}
Serial.println("SD card initialized successfully.");
digitalWrite(LED_PIN, LOW); // Turn off the LED after successful SD initialization.

// --- INA219 Check ---
// Try to initialize the INA219 sensor.
if (!ina219.begin()) {
  Serial.println("INA219 not found! Check I2C connections.");
  // If it fails, the LED blinks rapidly continuously (critical error).
  while (true) {
    digitalWrite(LED_PIN, HIGH); delay(50);
    digitalWrite(LED_PIN, LOW);  delay(50);
  }
}

// --- Prepare new data file on SD card ---
```

```
// It creates a unique filename (e.g., LOG00.CSV, LOG01.CSV)
// to avoid overwriting previous measurements.
for (int i = 0; i < 100; i++) { // Up to 100 files, from LOG00.CSV to LOG99.CSV
  sprintf(filename, "LOG%02d.CSV", i); // Formats the filename (e.g., LOG05.CSV).
  if (SD.exists(filename)) { // Checks if the file already exists.
    if (i == 99) { // If all 100 filenames are used, it starts overwriting from LOG00.CSV.
      Serial.println("Warning: Max 100 log files reached. Overwriting LOG00.CSV.");
      sprintf(filename, "LOG00.CSV");
      break;
    }
    continue; // If the file exists, move to the next filename.
  } else { // If the file doesn't exist, we've found a free filename.
    break;
  }
}

// Open the file with the found name. If it exists, it will be overwritten.
dataFile = SD.open(filename, FILE_WRITE);

if (dataFile) { // If the file opened successfully.
  dataFile.println("Sample,Time (ms),Divided Voltage (V)"); // Write the CSV header.
  dataFile.close(); // Close the file immediately after writing the header (important!).
  Serial.print("New file created: ");
  Serial.println(filename);
} else { // If the file failed to open.
  Serial.println("Error creating/opening log file! Data will not be saved.");
  // Indicate a critical error with rapid blinking.
  while(true) {
    digitalWrite(LED_PIN, HIGH); delay(100);
    digitalWrite(LED_PIN, LOW);  delay(100);
```

```
  }
 }

 // --- Wait 3 seconds before the experiment starts ---
 Serial.println("Waiting for 3 seconds before the experiment begins...");
 digitalWrite(LED_PIN, HIGH); delay(1000); // LED ON for 1 second.
 digitalWrite(LED_PIN, LOW);  delay(1000); // OFF for 1 second.
 digitalWrite(LED_PIN, HIGH); delay(1000); // ON for 1 second.
 digitalWrite(LED_PIN, LOW);  // OFF.

 // --- Experiment start signal (3 blinks: 1 second ON, 1 second OFF) ---
 // The LED blinks 3 times to signal the start of the timer.
 for (int i = 0; i < 3; i++) {
   digitalWrite(LED_PIN, HIGH); delay(1000); // Turn ON for 1 full second.
   if (i < 2) { // The LED doesn't need to turn off after the 3rd flash, before recording starts.
     digitalWrite(LED_PIN, LOW);  delay(1000); // Turn OFF for 1 second between flashes.
   }
 }
 // Total signal duration: 3 * 1000ms ON + 2 * 1000ms OFF = 5 seconds.

 recordingStartTime = millis(); // Start the 15-second timer.
 isRecording = true; // Set the flag to true, starting data recording.
 currentSampleCount = 0; // Reset the sample counter for the new run.

 Serial.println("Ready! Recording started for 15 seconds.");
 Serial.print("Sampling frequency: ~125 samples/second (one sample every ");
 Serial.print(SAMPLING_INTERVAL_MS);
 Serial.println(" ms)");
 digitalWrite(LED_PIN, LOW); // Turn off the LED to indicate active recording.
}
```

```
void loop() {
  // Checks if we are within the recording window
  if (isRecording && (millis() - recordingStartTime <
RECORDING_WINDOW_DURATION_MS)) {

    // Check if enough time has passed for the next sample (based on
SAMPLING_INTERVAL_MS).
    static unsigned long lastSampleTime = 0;
    if (millis() - lastSampleTime >= SAMPLING_INTERVAL_MS) {
      lastSampleTime = millis(); // Update the time of the last sample.

      // --- Collect Sample ---
      // We only measure the voltage as it reaches the INA219 input (after the voltage divider).
      float divided_voltage_read_by_INA219 = ina219.getBusVoltage_V();

      // --- Write directly to the SD card ---
      // Open the file for appending data (FILE_WRITE).
      File currentDataFile = SD.open(filename, FILE_WRITE);

      if (currentDataFile) { // If the file opened successfully
        currentDataFile.print(currentSampleCount); // Sample number.
        currentDataFile.print(",");
        currentDataFile.print(millis() - recordingStartTime); // Time since recording started (in
ms).
        currentDataFile.print(",");
        currentDataFile.println(divided_voltage_read_by_INA219, 3); // The measured voltage
with 3 decimal places.
        currentDataFile.close(); // Close the file (very important for SD cards).
        currentSampleCount++; // Increment the sample counter.

        // Visual indication: a very brief LED flash when a sample is taken and written.
```

```
      digitalWrite(LED_PIN, HIGH);
      digitalWrite(LED_PIN, LOW);
    } else { // If there is an error writing to the SD card.
      Serial.println("Error writing to SD card during recording!");
      // Indicate a critical error with rapid blinking.
      digitalWrite(LED_PIN, HIGH); delay(50);
      digitalWrite(LED_PIN, LOW);  delay(50);
      isRecording = false; // Stop recording if the write fails.
    }
  }
 } else if (isRecording) { // If the recording window has ended.
  Serial.println("Recording completed (15 seconds have passed).");
  isRecording = false; // Set the flag to indicate recording has stopped.

  // --- Final Flash & Halt Code ---
  Serial.println("Final flash and waiting for reset.");
  digitalWrite(LED_PIN, HIGH); delay(1000); // LED ON for 1 second (final flash).
  digitalWrite(LED_PIN, LOW);  // OFF.
  while(true); // The code halts here until the next reset.
 }

 // This part of the code will only be executed if the recording stops early due to an error.
 if (!isRecording) { // This will run if isRecording becomes false due to an error (before the timer ends).
  digitalWrite(LED_PIN, HIGH);
  delay(250); // Blinks every 0.5 seconds.
  digitalWrite(LED_PIN, LOW);
  delay(250);
 }

 // --- Serial Monitor Commands (Only works when connected to a computer) ---
```

```
  // This part of the code will only run if the code has not been halted by while(true);
  if (Serial.available()) {
    char cmd = Serial.read(); // Read the character the user sends.


    if (cmd == 'r') { // If the character is 'r'.
      Serial.println("--- Exporting Data from the SD Card ---");
      Serial.println("Sample,Time (ms),Divided Voltage (V)"); // Header for the export.
      File readDataFile = SD.open(filename, FILE_READ);
      if (readDataFile) { // If the file opened successfully for reading.
        String header_from_file = readDataFile.readStringUntil('\n'); // Read and discard the
first line (the actual file header).
        while (readDataFile.available()) { // Read and print all the remaining data from the file
byte by byte.
          Serial.write(readDataFile.read());
        }
        readDataFile.close(); // Close the file.
        Serial.println("--- End of Export ---");
      } else { // If there is an error opening the file for reading.
        Serial.print("Error opening ");
        Serial.print(filename);
        Serial.println(" for reading! The file may not exist or be corrupted.");
      }
    }
  }
}
```

MATLAB Code

```
close all
clear
clc
```

```
% informed by paper DOI 10.1007/s40430-016-0615-6
%
%% ROAD SPECTRUM per ISO 8608
%
% spatial frequency (n0) in cycles/meter
Omega0 = 1/2/pi;
% psd ISO
alpha=5; % use alpha = 1,2,3,4,5 for ISO road class A,B,C,D,E correspondingly
Sg_0 =  4^alpha * (10^-6);
% waveviness
n = 2;
%
%% Simulation parameters
%
% cyclic spatial frequency lower and upper limits (cycles/m)
Omega_L = 0.01;
Omega_U = 10;
% spectral decomposition resolution  (cycles/m)
delta_n = 0.001; % should be << Omega_L
% road length (m)
L = 3e3*delta_n/Omega_L;
% road station distance sampling (m)
dx=0.05; % should be <= 1/(2*Omega_U)
%
%% Setting up vectors for frequency, chosen PSD, decomposition amplitudes, road station
and iid uniform random angles
%
% spatial frequency band
Omega = Omega_L:delta_n:Omega_U;
%
%PSD of road
```

```
Sg = Sg_0.*(Omega./Omega0).^(-n);
%
% decomposition amplitudes
Amp = sqrt(2*Sg*delta_n);
%
% x abscissa from 0 to L (road station distance)
x = 0:dx:L;
%
% random phases
Psi = 2*pi*rand(size(Omega));
%
%% Generate random road elevation profile h (m)
%
h= zeros(size(x));
%
for i=1:length(x)
   hh=0;
   for j=1:length(Omega)
   hh=hh+ Amp(j)*cos(2*pi*Omega(j)*x(i) + Psi(j));
   end
   h(i)=hh;
end
%
figure
plot(x, h*1000 );
xlabel('Distance m');
ylabel('Elevation (mm)');
%
```

```
%% Compute PSD of generated profile for validation
grid on
figure
[q , C] = psd_1D(h, dx, 'x');  %
lambda = (2*pi) ./ q; % wavelengths
Omegaf = q / (2*pi); % spatial frequency
PSD = C; % power spectrum
loglog(Omegaf,PSD)
hold on
loglog(Omega,Sg/2/pi)
xlabel('spatial frequency (cycles/m)');
ylabel('PSD');
%
%% prepare for ANSYS
%
speed=18; % in (km/h)
v=speed/3.6; % in m/s
%
tt=x/v; % in s
%
dt=tt(2)-tt(1);
dtt=dt/5;
time=[tt(1):dtt:tt(end)]';
%
hf=spline(tt,1000*h',time);
index=length(find(time<1.2/v));
hr=hf;
hr(index+1:end)=hf(1:end-index);
hr(1:index)=hr(index+1);
%
```

```
function [q , C] = psd_1D(z, PixelWidth, dim)
% calculates averaged 1D PSD along x or y, for a surface height profile or
% simply for multiple 1D line profiles.
% It is better to remove mean and tilt in your topography/1D line profile,
% before applying this function
% examples:
% [q , C] = psd_1D(z, PixelWidth, 'x')
% [q , C] = psd_1D(z, PixelWidth, 'y')
% ===
% inputs:
% z: height topography (n*m) a matrix of n*m size (SI units, i.e. meters)
% or simply multiple 1D line profiles saved in a matrix; in the latter
% case, be careful on the input "dim" (explained below) which shows where
% your profiles are (in x direction or y direction)
% PixelWidth: size of each Pixel in topography/profile (SI units, i.e.
% meters). If you don't know your pixelwidth just devide topography/profile length by
% number of pixels in length.
% dim: direction of 1D PSD; 'x' or 'y':
% 'x' takes profiles that are parallel to x ; it means it assumes your
% height profiles are z(1,:), z(2,:),...., z(n,:)
% 'y' takes profiles that are parallel to y ; it means it assumes your
% height profiles are z(:,1), z(:,2),...., z(:,m)
% Note That : [n , m ] = size (z);
% ===
% outputs:
% q: wavevectors, which is 2pi/lambda. lambda is wavelength of your
% roughness components. If you are not familiar with concept, refer to the
% appendix in below article to get insight into calculation procedure:
% "Persson, B. N. J., et al. "On the nature of surface roughness with application
% to contact mechanics, sealing, rubber friction and adhesion." Journal of Physics:
```

```
% Condensed Matter 17.1 (2005): R1."
% C: 1D PSD averaged for multiple line profiles
% in order to plot final result just use:
% loglog(q,C)
%
=========================================================================
===
% Check number of inputs
if nargin ~=3
   error('The code requires exactly 3 inputs. Check code description.');
end
%
=========================================================================
===
if strcmp(dim ,'y')
   z = z';
end
[n,m] = size(z);
a = PixelWidth; % lattice spacing
%
=========================================================================
===
% Window function just in one direction
win = ones(n,1) * (1 - (((0:m-1)-((m-1)/2))/((m+1)/2)).^2); % Welch
% win = ones(n,1) * bartlett(m)';
% win = ones(n,1) * tukeywin(m,0.1)';
z_win = z.* win;
%
=========================================================================
===
% Normalization factor (due to window function)
U = sum(win(1,:).^2)/((m-1));
```

```
%
=========================================================================
===
% Calculate 1D PSD
Hm = fft(z_win , [] , 2); % fft of all rows
Cq = (1/U).*((a/m)*(1/(2*pi))).*((abs(fftshift(Hm,2))).^2);
%
=========================================================================
===
% corresponding wavevectors to Cq values after fftshift has been applied
q_1=zeros(m,1);
for k=0:m-1
    q_1(k+1)=(2*pi/m)*(k);
end
q_2 = fftshift(q_1);
q_3 = unwrap(q_2-2*pi);
q = q_3/a;
C = mean(Cq , 1)';
%
end
```